SPECIAL PECAN COLLECTION

The Great Plains Low-Level Jet during PECAN: Observed and Simulated Characteristics

ELIZABETH N. SMITH

School of Meteorology, and Cooperative Institute for Mesoscale Meteorological Studies, University of Oklahoma, Norman, Oklahoma

JOSHUA G. GEBAUER, PETRA M. KLEIN, AND EVGENI FEDOROVICH

School of Meteorology, University of Oklahoma, Norman, Oklahoma

JEREMY A. GIBBS

Department of Mechanical Engineering, University of Utah, Salt Lake City, Utah

(Manuscript received 16 August 2018, in final form 20 February 2019)

ABSTRACT

During the 2015 Plains Elevated Convection at Night (PECAN) field campaign, several nocturnal low-level jets (NLLJs) were observed with integrated boundary layer profiling systems at multiple sites. This paper gives an overview of selected PECAN NLLJ cases and presents a comparison of high-resolution observations with numerical simulations using the Weather Research and Forecasting (WRF) Model. Analyses suggest that simulated NLLJs typically form earlier than the observed NLLJs. They are stronger than the observed counterparts early in the event, but weaker than the observed NLLJs later in the night. However, sudden variations in the boundary layer winds, height of the NLLJ maximum and core region, and potential temperature fields are well captured by the WRF Model. Simulated three-dimensional fields are used for a more focused analysis of PECAN NLLJ cases. While previous studies often related changes in the thermal structure of the nocturnal boundary layer and sudden mixing events to local features, we hypothesize that NLLJ spatial evolution plays an important role in such events. The NLLJ is shown to have heterogeneous depth, wind speed, and wind direction. This study offers detailed documentation of the heterogeneous NLLJ moving down the slope of the Great Plains overnight. As the NLLJ evolves, westerly advection becomes significant. Buoyancy-related mechanisms are proposed to explain NLLJ heterogeneity and down-slope motion. Spatial and temporal heterogeneity of the NLLJ is suggested as a source of the often observed and simulated updrafts during PECAN cases and as a possible mechanism for nocturnal convection initiation. The spatial and temporal characteristics of the NLLJ are interconnected and should not be treated independently.

1. Introduction

Wind maxima called nocturnal low-level jets (NLLJs) often occur during the night in the lowest kilometer of the atmosphere. In the most general sense, the NLLJ is the result of the disruption of the daytime force balance between the Coriolis, pressure gradient, and frictional forces. Once the sun sets, thermally generated turbulence decays, and the stable boundary layer (SBL) forms. The frictional force weakens above the surface, which eliminates the force balance and leads to increased wind speed in the boundary layer (e.g., Blackadar 1957). While NLLJs are observed in many locations around the globe such as the Koorin Jet (e.g., Brook 1985) and Southerly Buster (e.g., Baines 1980) in Australia and the Somali Jet of East Africa (e.g., Ardanuy 1979), our study focuses on NLLJs that commonly form over the Great Plains of the United States, especially in the warm months, and are usually southerly (e.g., Blackadar 1957; Bonner 1968; Zhong et al. 1996; Whiteman et al. 1997; Banta et al. 2002; Song et al. 2005; Banta 2008; Klein et al. 2016).

Corresponding author: Elizabeth N. Smith, elizabeth.n.smith@ou.edu

DOI: 10.1175/MWR-D-18-0293.1

These NLLJs can modulate the atmosphere in many ways resulting in weather and climate impacts for the region (Stensrud 1996). The southerly NLLJ can transport moisture from the Gulf of Mexico over the central United States. This transport has been connected to the observed nocturnal maximum in warm-season precipitation in this part of the country (Markowski and Richardson 2010). The NLLJ can modify the thermodynamic and dynamic structure of the lower atmosphere in support of convection initiation and severe weather (Pitchford and London 1962; Bonner 1966; Maddox 1983; Astling et al. 1985; Trier et al. 2006; Fedorovich et al. 2017; Gebauer et al. 2018). The NLLJ can also impact aviation, wind energy, and pollution transport (e.g., Hu et al. 2013; Klein et al. 2014).

Early climatology showed that NLLJ wind maxima in the Great Plains have an average height of 800 m above ground level (AGL) (Bonner 1968), while more recent studies using higher-resolution data showed that the NLLJ maximum often occurs below 500 m AGL (Whiteman et al. 1997; Song et al. 2005). Winds associated with NLLJs are often very strong and can reach magnitudes nearly double that of daytime boundary layer wind (Shapiro and Fedorovich 2010). In addition to the practical significance of the NLLJ, it remains a challenging fluid dynamical phenomenon due to incomplete understanding of its associated physical mechanisms. Various theories in the literature have attempted to describe the NLLJ (Blackadar 1957; Wexler 1961; Holton 1967). However, a complete theory that fully describes the phenomenon as seen in observations has yet to be developed. Given the slope of the Great Plains, NLLJs in this part of the world can be complicated by radiative heating and cooling of the sloping terrain (e.g., Holton 1967), buoyancy effects (e.g., Shapiro and Fedorovich 2009), or a combination of various factors (e.g., Shapiro et al. 2016). Recent studies by Parish (2017) and Fedorovich et al. (2017) link the prevalence of the NLLJ in the Great Plains to slope effects. While Parish (2017) identified the thermal wind forcing and related horizontal pressure gradient over the sloping terrain of the Great Plains as key mechanisms for NLLJ formation, Fedorovich et al. (2017) highlighted the role of along-slope temperature advection in modulating the NLLJ structure.

Gaps in our understanding of the NLLJ may be connected to gaps in our understanding of the nocturnal boundary layers (NBLs) in which they form. Many studies attempted to connect NLLJ characteristics to near-surface features of atmospheric flow. Using CASES-99 data, Banta et al. (2002) and Banta et al. (2003) related NLLJ characteristics including wind speed, height of wind maximum, wind direction, a measure of sub-NLLJ shear, and an NLLJ Richardson number to mixing and turbulence across the NBL. Later work expanded such relations to analysis of stability effects (Banta et al. 2006). Banta (2008) connected strong NLLJs to continuous turbulence and weak NLLJs to intermittent turbulence with an intermediate range between the two extremes. Changing stability in the NBL has been linked to advection of thermodynamic properties by the NLLJ (Bonin et al. 2015), and intermittent turbulence bursting events have been linked to changing stability (Ohya et al. 2008). More direct connections between wind speed in the nocturnal boundary layer and turbulence regimes were found in Sun et al. (2012), where a threshold wind speed was identified to maintain turbulence. Klein et al. (2016) found correlations between NLLJs and daytime stability and turbulence, but weak to no relationship between NLLJs and nighttime stability and turbulence.

Several of the aforementioned studies found that near-surface flow parameters alone were often not representative of the changes observed in the NLLJ and the NBL. Classification of NLLJs based on the turbulence state of the environment in which they formed showed that NLLJ evolution is different for strongly turbulent and weakly turbulent NLLJ cases (Bonin et al. 2019, manuscript submitted to *Bound.-Layer Meteor.*). Banta et al. (2003) found the relationships between turbulence and NLLJs did not hold well in very stable boundary layers. Later work indicated that the top-down generation of turbulence, or upside down boundary layer, limited the validity of traditional boundary layer scaling approaches (i.e., scaling based on the friction velocity u_* was not as useful as scaling based on the NLLJ wind speed) suggesting that local surface features may not be as important for understanding NLLJ characteristics and evolution (Banta et al. 2006). Furthermore, Banta (2008) speculated that in stable cases some turbulent bursting events may be more connected to what he called imported disturbances. The lack of correlation between NLLJ features and nighttime stability and turbulence in Klein et al. (2016) also suggests that NLLJ evolution throughout the night may not be well represented by local NBL characteristics.

Traditional approaches used in the literature to understand NLLJs are often limited by the available observations which are typically confined to towers erected on Earth's surface or single point observations. This limitation can be addressed in two ways: 1) using three-dimensional numerical simulations and 2) performing more extensive observations covering a broader domain. Previous numerical studies have provided additional insights into the Great Plains NLLJ. Soil moisture changes were shown to impact NLLJ amplitude by Zhong et al. (1996). Pan et al. (2004) explored the connection between

NLLJ formation and slope-induced horizontal temperature gradients. Fedorovich et al. (2017) used direct numerical simulations to investigate the NLLJ life cycle and found substantial dependence on the free-atmospheric geostrophic wind, ambient atmospheric stratification, surface buoyancy forcing, atmospheric turbulence, and slope angle. Nonetheless, past numerical modeling studies have consistently shown that representing the evolving NBL and embedded NLLJs is not easily accomplished in mesoscale models, partly due to the poor performance of turbulence parameterizations applied in boundary layer schemes. NLLJ magnitude and depth are often underestimated in studies with different boundary layer parameterization schemes in the Weather Research and Forecasting (WRF) Model (Skamarock et al. 2008; Storm et al. 2009). Considering NLLJ predictions by three state-of-the-art mesoscale models, Steeneveld et al. (2008) found consistent underestimation of the NLLJ in their simulations. However, more recent efforts have shown progress in achieving better agreement between observed and simulated NLLJ features using the WRF Model (e.g., Vanderwende et al. 2015; Mirocha et al. 2016; Klein et al. 2016). Successful representation of the NLLJ benefits from model parameter tuning specific to the application at hand; for improving NLLJ simulations, grid spacing and boundary layer parameterization considerations are particularly important (Mirocha et al. 2016; Smith et al. 2018).

Observations and simulations each have their own inherent limitations. Observations are limited to the spatial and temporal coverage and resolution of the deployed measurement platforms. The Plains Elevated Convection at Night (PECAN; Geerts et al. 2017) observations provide vertical profiles of kinematic and thermodynamic variables at several point locations with prescribed frequency (usually on the order of 2–5 min). While the PECAN dataset offers high-quality, extensive spatial and temporal observations of the NLLJ, these observations still cannot provide information beyond these set points. Numerical simulations are not as limited in space and time as observations. Depending on the available computational resources, simulations can provide data on fine temporal and spatial scales. However, simulations are limited by the ability of the model to represent key atmospheric properties and phenomena on a required range of scales. Additionally, simulation outcomes are dependent on the quality of initialization data. Even the best models will not produce reliable predictions if the initial or forcing data do not accurately represent the events of interest.

Observations constitute one mechanism to evaluate a model's performance, while simulations extend the considered range of atmospheric scales beyond those allowed by observations alone. Using observations and simulations in tandem provides opportunities for more robust analyses than possible when using just one or the other. In this study, the PECAN observations are employed in two ways: first, the data are used to confirm the utility of the optimal WRF Model configuration identified in previous NLLJ studies (Smith et al. 2018). Second, they are jointly analyzed with WRF Model data to advance understanding of NLLJ physical processes. The employed data and methods are described in the following section. Then a summary of the cases of interest is presented followed by an evaluation of the model's performance. Using simulated and observed data, NLLJ physical processes are discussed next. Summary and conclusions are presented in the final section.

2. Data and methods

The PECAN field campaign was an international project funded by the National Science Foundation, the National Oceanic and Atmospheric Administration, the National Aeronautics and Space Administration, and the Department of Energy (Geerts et al. 2017). Measurements were collected from 1 June to 15 July 2015 over a 9-state region during 31 intensive operational periods (IOPs) and 12 unofficial field operations. The primary goal of PECAN was to better understand nocturnal convection. Several important components related to nocturnal convection were identified for detailed study: mesoscale convective systems, bores, convection initiation, and NLLJs. Primary data sources for NLLJ cases were the boundary layer profiles measured by mobile and fixed PECAN Integrated Sounding Arrays (PISAs). These datasets included profiles of dynamic and thermodynamic parameters obtained at high temporal and vertical resolution using Doppler lidars, Atmospheric Emitted Radiance Interferometers (AERIs), radar wind profilers, radiosondes, and microwave radiometers (MWRs), providing observations to describe the SBL and NLLJ evolution. There were four mobile PISAs (MPs) roaming the domain on a mission by mission basis, and six fixed PISA (FP) sites dispersed across the PECAN domain in Kansas, Oklahoma, and Nebraska collecting data nearly continuously. Based on the target of a given mission, the positioning of PECAN MPs and other mobile assets were highly variable. As such, we focus only on NLLJ targeted missions, which used consistent MP locations. For NLLJ IOPs, these PISA sites provided information about the spatial variability and evolution of the SBL and NLLJ that has historically been unavailable. The PECAN observational domain and the locations of

FPs and MPs (for a typical NLLJ deployment) are shown in Fig. 1.

The University of Oklahoma (OU) and the National Severe Storms Laboratory (NSSL) maintain an instrumentation platform called the Collaborative Lower Atmospheric Mobile Profiling System (OU/NSSL-CLAMPS), which operated during PECAN as MP1. Greensburg, Kansas, hosted the FP2 site, and Ellis, Kansas, hosted FP3. These three sites comprise a north–south-oriented transect on which NLLJ observations were evaluated. This transect was chosen because all sites included Doppler lidars and AERIs, and data quality was good. At MP1, FP2, and FP3, a scanning Doppler lidar conducted profile observations of the wind field including plan position indicator (PPI) scans and periods of staring vertically to sample the horizontal and vertical wind, respectively (Turner 2016c,d; Delgado et al. 2015; Hanesiak and Turner 2016). The Doppler lidar data were passed through a signal-to-noise ratio (SNR) check for validity. Following the analysis in Päschke et al. (2015), we determined that a threshold of SNR $< 0.01 = -20$ dBZ was acceptable for removing noisy data and providing reasonable data availability. Then, the data were only used in the analysis if the error in retrieval from the velocity–azimuth display (VAD) technique performed on PPI scans was low. These procedures typically removed data where the lidar return signal was weak. If they were not already removed, the lowest 100 m of the lidar data were also removed for quality purposes as this region was often too near the lidar to produce trustworthy results. The scan patterns and characteristics of the resulting Doppler lidar data from each site are summarized in Table 1. Each site also had an AERI, which observed the radiance spectra used to retrieve thermodynamic profiles (Turner 2016b, a, 2015) with 5-min temporal resolution. Information about the retrieval method is available in Turner and Löhnert (2014).

Using observational data similar to those collected during PECAN, Smith et al. (2018) identified an optimal WRF Model configuration for reproducing the Great Plains NLLJ. The considered tests included analyses of the effects of horizontal grid spacing, vertical grid spacing, and planetary boundary layer (PBL) scheme. The optimal grid configuration was identified as a nonnested numerical mesh with 4-km horizontal grid spacing and nonstretched 40-m vertical grid spacing. Improvements in the simulation associated with using nested domains and finer horizontal spacing did not justify the increased computational cost. While performance evaluation parameters in Smith et al. (2018) were similar for simulations with three different PBL schemes, the QNSE PBL scheme (Sukoriansky et al. 2005) was found optimal for reproducing principal features of NLLJ evolution and thermal structure of the NBL. Likewise, Mirocha et al. (2016) also saw slightly improved overall performance using the QNSE scheme relative to the others. Accordingly, simulations in the present study used the same configuration with the QNSE scheme. The simulation domain was centered on Hays, Kansas, and was configured such that it fully encompassed the entire PECAN observation domain as shown in Fig. 1. Details of the WRF Model configuration are listed in Table 2.

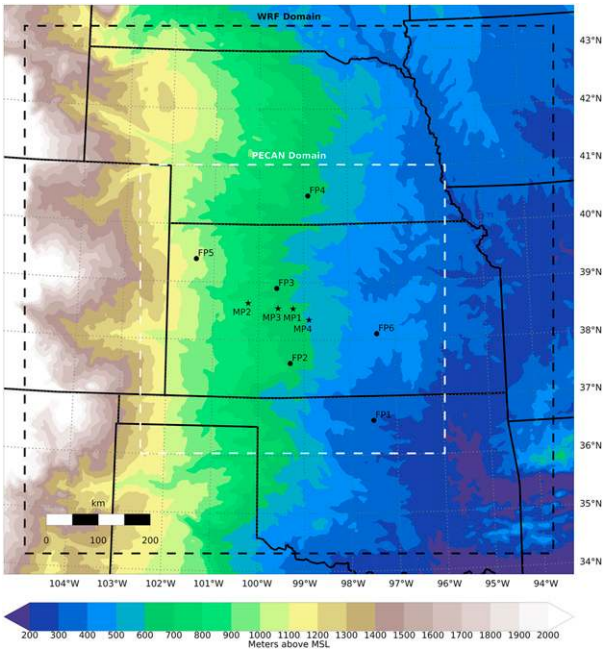

FIG. 1. Geographical depiction of the observational domain, simulation domain, and the fixed PISA (FP; circles) and mobile PISA (MP; stars) observing platforms overlaid on the region's terrain height.

To compare the PECAN observations with the WRF Model output, model data from the four nearest grid cells to the observation location were spatially averaged to generate a representative modeled vertical profile. Time–height cross sections from the resulting modeled vertical profiles were compared with time–height cross sections of the observed data. Simple visual comparison provided information about the ability of the WRF Model to reproduce NLLJs with similar characteristics as those observed during PECAN, supporting the verification results presented in Smith et al. (2018). These comparisons included wind characteristics and thermodynamic variables. Model performance was also assessed by examining the height of the NLLJ maximum and the position of the core region, where the wind speed is 90% of the maximum wind speed.

TABLE 1. Characteristics of various Doppler lidar data used in this study.

	FP3 (Hanesiak and Turner 2016)	MP1 (Turner 2016d)	FP2 (Delgado et al. 2015)
Scan strategy	Continuous Doppler beam swing	70° VAD–stare	5-elevation VAD–stare
Scan cycle time	15 s	3 min	24 min
Vertical resolution	50 m	30 m	10 m
Lowest range gate	100 m	28 m	10 m

The comparisons shown herein are not meant as an exercise in quantitative verification, but are included to confirm the utility of the previously identified optimal WRF Model configuration. To assess the spatial evolution and horizontal heterogeneity of the NLLJ, time–height cross sections were compared for different locations across the PECAN domain. Additionally, plan view patterns and vertical cross sections were evaluated to better understand the temporal and spatial characteristics of the NLLJ.

3. PECAN NLLJ IOPs

PECAN IOP02, IOP12, and IOP13 are considered in this study. All three IOPs were NLLJ specific missions. It is worth noting that IOP07 was also a NLLJ specific mission, but CLAMPS/MP1 was not fully operational during that night, so IOP07 data are not included here. In all three IOPs, CLAMPS/MP1 was deployed just east of La Crosse, Kansas (see Fig. 1). Each NLLJ case can be classified as a weakly turbulent NLLJ based on observed vertical velocity variance and follows the expected synoptic patterns (no strong trough to the west with generally weak synoptic forcing and slowly increasing pressure gradients overnight) for weakly turbulent NLLJs described in Bonin et al. (2019 manuscript submitted to *Bound.-Layer Meteor.*).

IOP02 took place from 0000 to 0600 UTC 3 June 2015. On this night, a low pressure system was located over the central-eastern contiguous United States (CONUS) with a high-amplitude trough–ridge extending to the Midwest. On the upstream side of the associated ridge, the PECAN domain was under mostly zonal flow at the upper and midlevels with a weak northerly component. Closer to the surface, flow was southerly turning southwesterly by 1200 UTC. Conditions overnight were approximately stationary on the synoptic scale. A more detailed discussion of the synoptic conditions for this case can be found in Parish (2016). A NLLJ was observed beginning around 0100 UTC, with the wind maximum at a height between 400 m and 500 m AGL. The maximum strength of the NLLJ was nearly 25 m s^{-1} (Figs. 2b,d; 3b,d; 4b,d).

IOP12 took place from 0000 to 1000 UTC 20 June 2015. A low pressure system was again located over the eastern United States, but a bit farther west than during IOP02. On this night, a trough was present to the east, but was not as high amplitude as during IOP02. This trough gave way to weak zonal flow over the PECAN domain at upper levels. Midlevels were more impacted by the proximity of the low pressure on this night, but flow was still mostly zonal. The near-surface flow had a stronger westerly component than during IOP02. Again, synoptic conditions, discussed in more detail in Parish and Clark (2017), were fairly stationary overnight. The NLLJ developed similarly to the NLLJ on IOP02 (Figs. 2f,h; 3f,h; 4f,h). This case was unique as it was characterized by peculiar diagonal striations in in the time–height wind speed profile observed throughout the night (Fig. 5).

IOP13 took place from 0000 to 1000 UTC 22 June 2015. That night was characterized by zonal flow over most of the CONUS. This synoptic flow pattern was different than the ridge–trough patterns during IOP02 and IOP12 and led to very warm conditions over the Great Plains. Upper- and midlevel flow over the area of interest was zonal through the night, and near surface flow was southerly turning southwesterly in time. This NLLJ formed at a similar time and height as those during IOP02 and IOP12, but was stronger and deeper than in those two cases. This NLLJ was the strongest of the three cases considered

TABLE 2. Summarized settings for the WRF Model used in this study.

WRF version	3.8.1
Initial and boundary condition model	NAM 12 km, 6-h updates
Spinup time	24 h prior to 0000 UTC on date of interest
Domain	256 × 256 × 256 centered on Hays, Kansas
Horizontal grid	Nonnested 4-km spacing
Vertical grid	Nonstretched 40-m spacing (first level: 20 m, top level: 10 220 m)
Microphysics	Ferrier scheme
Longwave radiation	RRTM scheme
Shortwave radiation	Dudhia scheme
Surface layer	Unified Noah land surface model
Boundary layer	Quasi-normal scale elimination scheme (with QNSE surface layer scheme)
Cumulus	No cumulus option

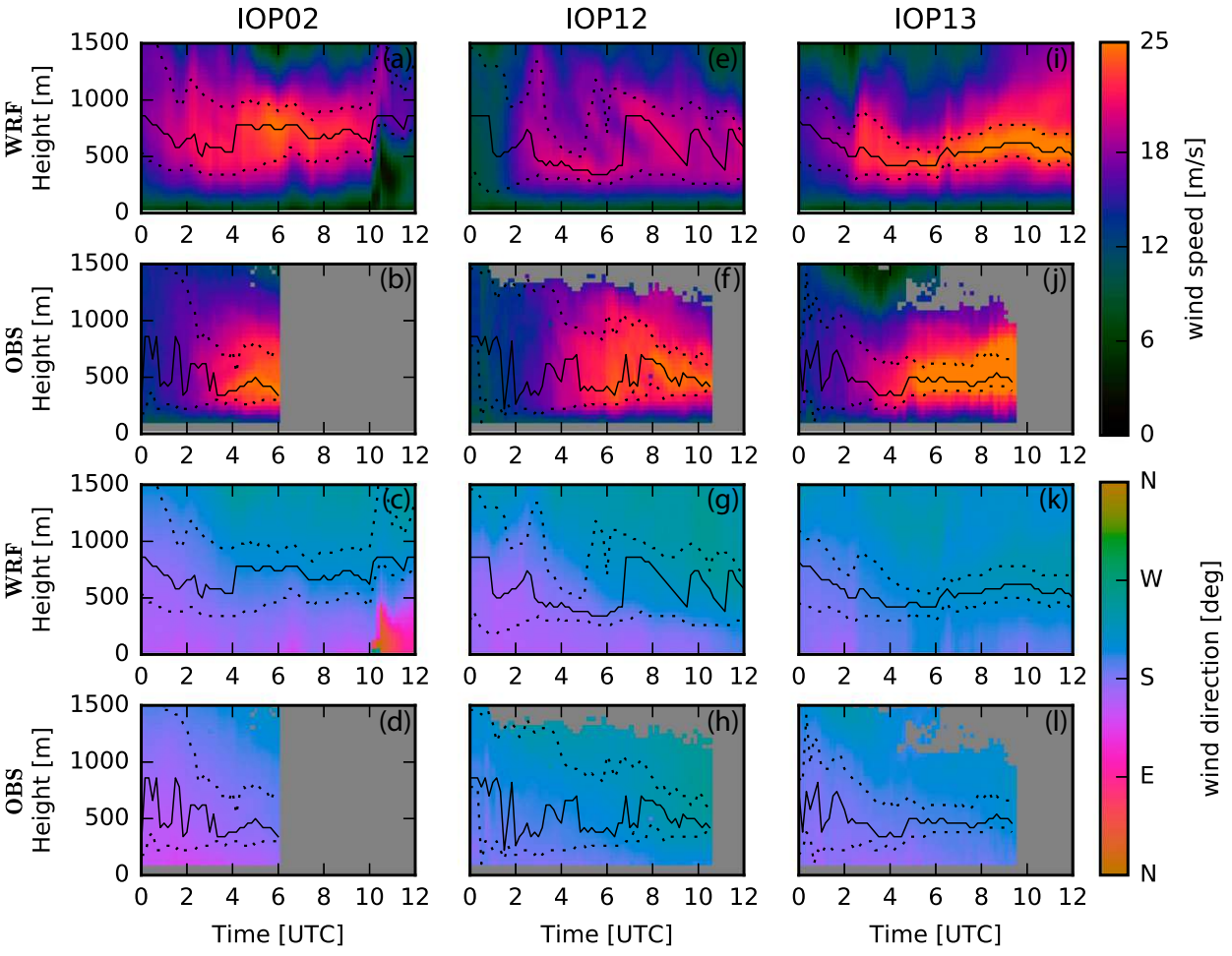

FIG. 2. Observed and simulated wind speed and wind direction are shown at MP1 for IOP02, IOP12, and IOP13. Gray areas indicate observations are unavailable or omitted for quality purposes. Solid lines indicate the height of the NLLJ maximum, and the dotted lines encompass the core region, where the wind speed is at least 90% of the NLLJ maximum. For reference, sunset occurred near 0200 UTC (2100 CDT) and sunrise occurred shortly after 1100 UTC (0600 CDT). MP1 observations are available in Turner (2016c).

in this study with a maximum magnitude near 30 m s^{-1} (Figs. 2j,l; 3j,l; 4j,l).

4. Model evaluation

Figure 2 shows simulated (Figs. 2a,e,i) and observed (Figs. 2b,f,j) wind speed at MP1. Analogous data are presented in Figs. 3 and 4 for FP2 and FP3, respectively. At MP1, the NLLJs reproduced by the WRF Model formed about two hours earlier than those observed by lidar (Fig. 2a). The height of the NLLJ maximum assessed from lidar data was uncertain during the early portion of IOP02 due to ongoing mixing within the boundary layer (Fig. 2b). Evidence of such mixing was not present in the WRF Model output, which may explain premature NLLJ formation. The vertical structure of the NLLJ was realistically reproduced by the WRF Model, including the diagonal striations—a signature in time–height wind speed profiles where the location of the max velocity descends quickly—present during IOP12 (Figs. 5d–f). Similar to results for MP1, the NLLJ was observed to develop later than the WRF Model prediction at FP2; however, the difference in magnitude between observations and simulations was smaller at FP2 than at MP1. The diagonal striations noted at MP1 were also observed and simulated at FP2, but at a later time (Fig. 5f), and the NLLJ height and core region were again well represented. Results at FP3 mirrored those for FP2 and MP1, except that the WRF Model more severely underestimated observed NLLJ magnitude at this site. Data at FP3 for IOP02 are affected by storms outside the area of interest producing outflow, which approached the location too early in the simulation. This behavior is clearly seen in Fig. 4a after 0900 UTC.

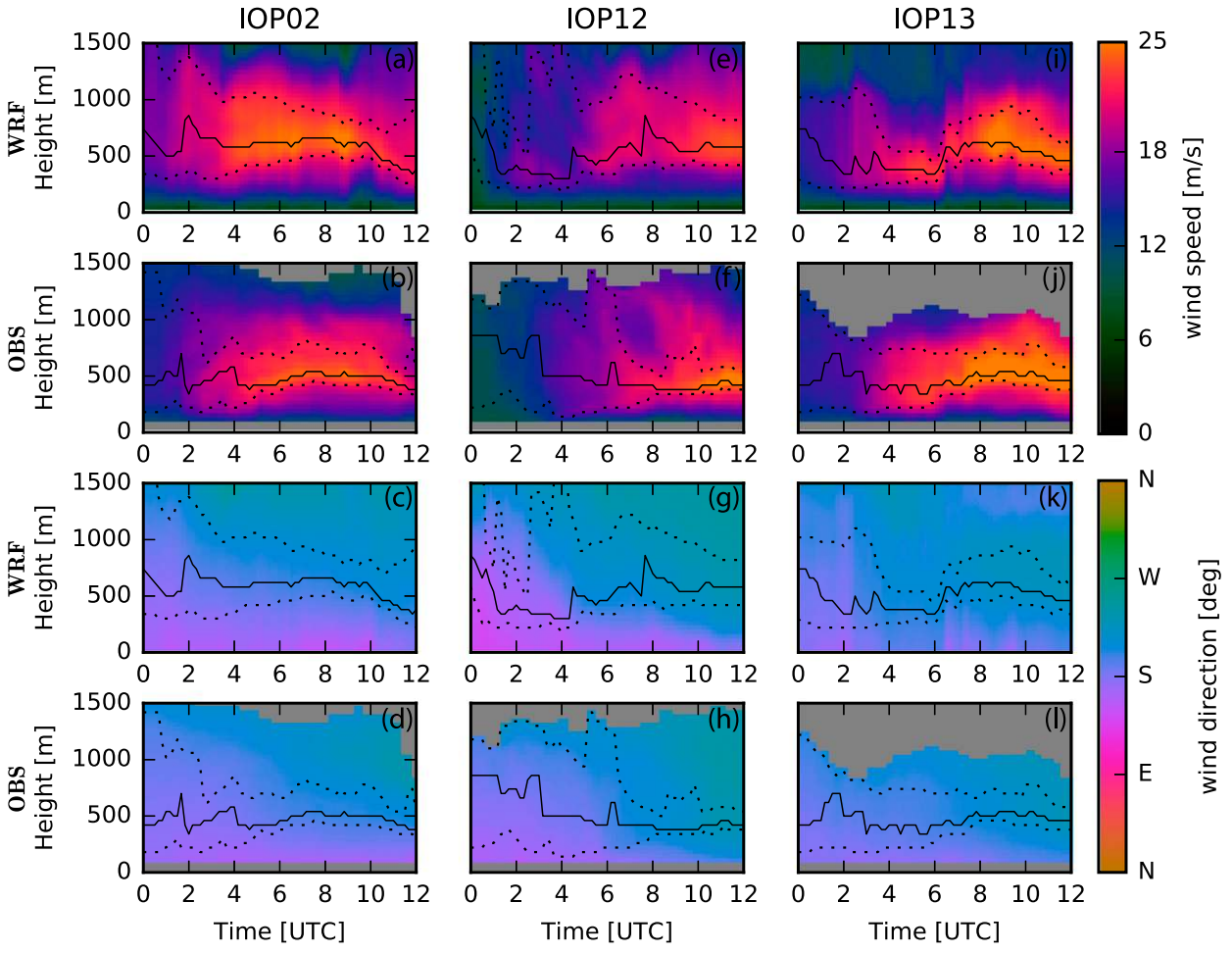

FIG. 3. As in Fig. 2, but for site FP2. For reference, sunset occurred near 0200 UTC (2100 CDT) and sunrise occurred shortly after 1100 UTC (0600 CDT). FP2 observations are available in Delgado et al. (2015).

Overall, the structure and evolution of the NLLJ were well captured in the simulations. Figures 2, 3, and 4 also show simulated (Figs. 2c,g,k; 3c,g,k; 4c,g,k) and observed (Figs. 2d,h,l; 3d,h,l; 4d,h,l) wind direction. Generally speaking, the wind direction was well reproduced by the simulations as compared with observations at all sites, except for the case of the mistimed outflow at FP3 late in IOP02.

Each NLLJ simulated by the WRF Model was too strong early in the night and too weak once fully developed. This behavior is well documented in the literature, with many studies showing underestimation of NLLJ magnitude and depth (e.g., Storm et al. 2009; Steeneveld et al. 2008; Vanderwende et al. 2015; Mirocha et al. 2016; Klein et al. 2016). However, underestimation of NLLJ magnitude and depth in the simulations used in this study was relatively small (usually less than $5\,\mathrm{m\,s^{-1}}$.) Simulations misrepresent the NLLJ magnitude at FP3 (Fig. 4) more so than at FP2 and MP1 (Figs. 3 and 2). Reasons for this misrepresentation are unclear, but could be related to site characteristics not represented by the model, poor performance of the employed boundary layer parameterizations, or caused by unknown observation biases.

The depth of the NLLJ was well reproduced in the simulations, as can be seen by comparing the core region enclosed by dashed lines in all panels of Figs. 2, 3, and 4. At any given time, the height of the NLLJ or the depth of the core region may have matched imperfectly, but the general evolution of the simulated and observed NLLJ was similar. In addition to representing the NLLJ magnitude and height well, the WRF Model also captured the sudden variations in observed boundary layer winds. For example, while the simulated wind speed was weaker than observed at each site during IOP12, the simulation depicted the characteristic diagonal striation signatures in the time–height wind profiles similar to those found in the observations.

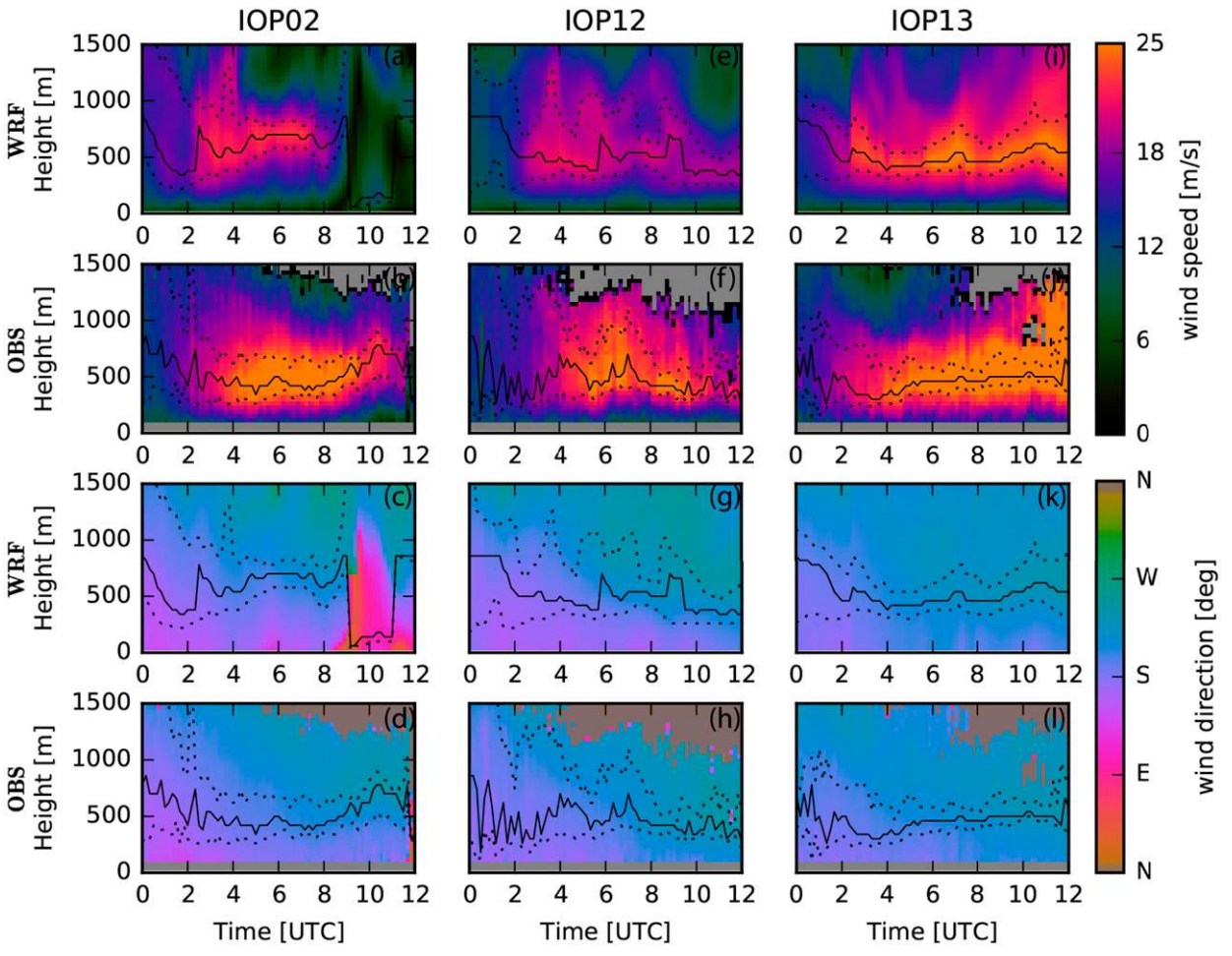

FIG. 4. As in Fig. 2, but for site FP3. For reference, sunset occurred near 0200 UTC (2100 CDT) and sunrise occurred shortly after 1100 UTC (06 CDT). FP3 observations are available in Hanesiak and Turner (2016).

These diagonal striation features will be explored in the next section.

Figures 6, 7, and 8 show simulated (Figs. 6a,e,i; 7a,e,i; 8a,e,i) and observed (Figs. 6b,f,j; 7b,f,j; 8b,f,j) vertical velocity. Because of differences in scan strategies at each site, the temporal resolution and length of vertical stare data from Doppler lidars varied. To allow for better comparison between sites, the various vertical stares were all averaged into 15-min bins for this analysis. Sudden instances of vertical motion were observed during several PECAN NLLJ cases at numerous sites. While the magnitudes of the vertical velocity in these updrafts were small, they were nevertheless measurable bursts of vertical motion. Such updrafts were also present in the WRF Model output. Although the timing was imperfect, the basic updraft features were similar between the observations and the simulations. The observed and simulated updrafts were not as strong or frequent at FP2 as compared with the updrafts at MP1. At FP3, vertical velocity observations and simulations revealed similar updrafts as those present at MP1. The nature of these updrafts will be discussed in greater detail below.

Figures 6, 7, and 8 also show simulated (Figs. 6c,g,k; 7c,g,k; 8c,g,k) and observed (Figs. 6d,h,l; 7d,h,l; 8d,h,l) potential temperature fields. Overall the general pattern of potential temperature evolution was well represented in the simulations. One particularly interesting result is evident when focusing on the later portions of the nights at MP1 (Fig. 6). After approximately 0600 UTC, the near-surface air cools substantially. At the same time, the layer above the jet maximum warms. This simultaneous near-surface cooling and warming aloft, found in both the observations and simulations, results in a stronger temperature gradient in the NLLJ core region. At MP1, this feature is more readily seen in IOP12 and IOP13 observations because data collection at the mobile PISAs stopped earlier during IOP02. The AERI

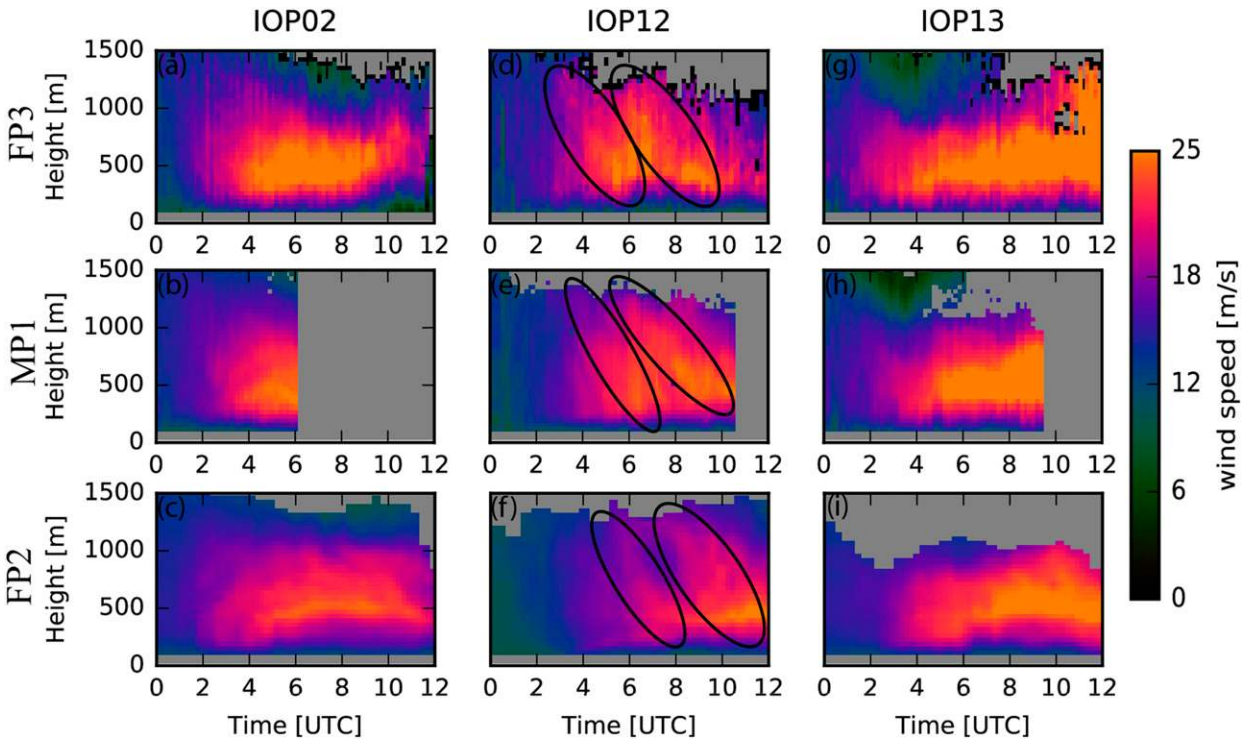

FIG. 5. Wind speed observations from (a),(d),(g) FP3, (b),(e),(h) MP1, and (c),(f),(i) FP2 are reproduced with diagonal striations during IOP12 highlighted by black circles. For reference, sunset occurred near 0200 UTC (2100 CDT) and sunrise occurred shortly after 1100 UTC (0600 CDT).

was not yet fully operational at FP2 during IOP02 (thus, the thermodynamic observations are lacking). Otherwise, simulated potential temperature fields appeared similar to those observed at this site. The cooling of the surface layer and the warming aloft were again well represented by the simulation. Potential temperature data from simulations and observations matched well at FP3 if, again, considerations are made for the mistimed outflow during IOP02. The cause of observed warming above the NLLJ will also be explored in the next section.

5. NLLJ physics

To better understand the evolution of the NLLJ, the nocturnal jet from IOP12 is chosen for further detailed analysis. IOP12 has good data availability, and shows features of heterogeneous NLLJ morphology including observed and simulated diagonal striation signatures and sudden bursts of vertical motion. PECAN observations from IOP12 along the north–south transect are shown in Figs. 2–4 and 6–8. Potential temperature observations show the SBL deepening overnight while warming occurred above the NLLJ. Sudden vertical motions were observed and often coincided with diagonal striation signatures in the wind speed time–height profiles.

As discussed in section 1, observed sudden mixing events have often been related to possible shear-generated turbulence as the jet strengthens (e.g., Banta et al. 2002, 2003; Banta 2008; Sun et al. 2012). However, the PECAN observations from IOP12 showed mean (rather than turbulent) motions over a rather thick layer that seemingly coincided with changes in NLLJ structure above its nose resulting in diagonal striation signatures in the time–height wind profiles. These signatures were observed at several locations at different times. We hypothesize that the spatial evolution of the NLLJ rather than locally driven changes in shear plays an important role in local NLLJ heterogeneity. More specifically, local changes in shear are likely an aspect of the NLLJ evolution. However, with PECAN observations limited to only a few locations in space, the spatial features cannot be explored in more detail using observations alone. Three-dimensional flow fields from the WRF Model are examined to afford additional insight about NLLJ evolution in time and space. Since the optimally configured WRF Model produced NLLJs that were generally representative of the observed features of the NLLJ at MP1, FP2, and FP3 in all three cases discussed above

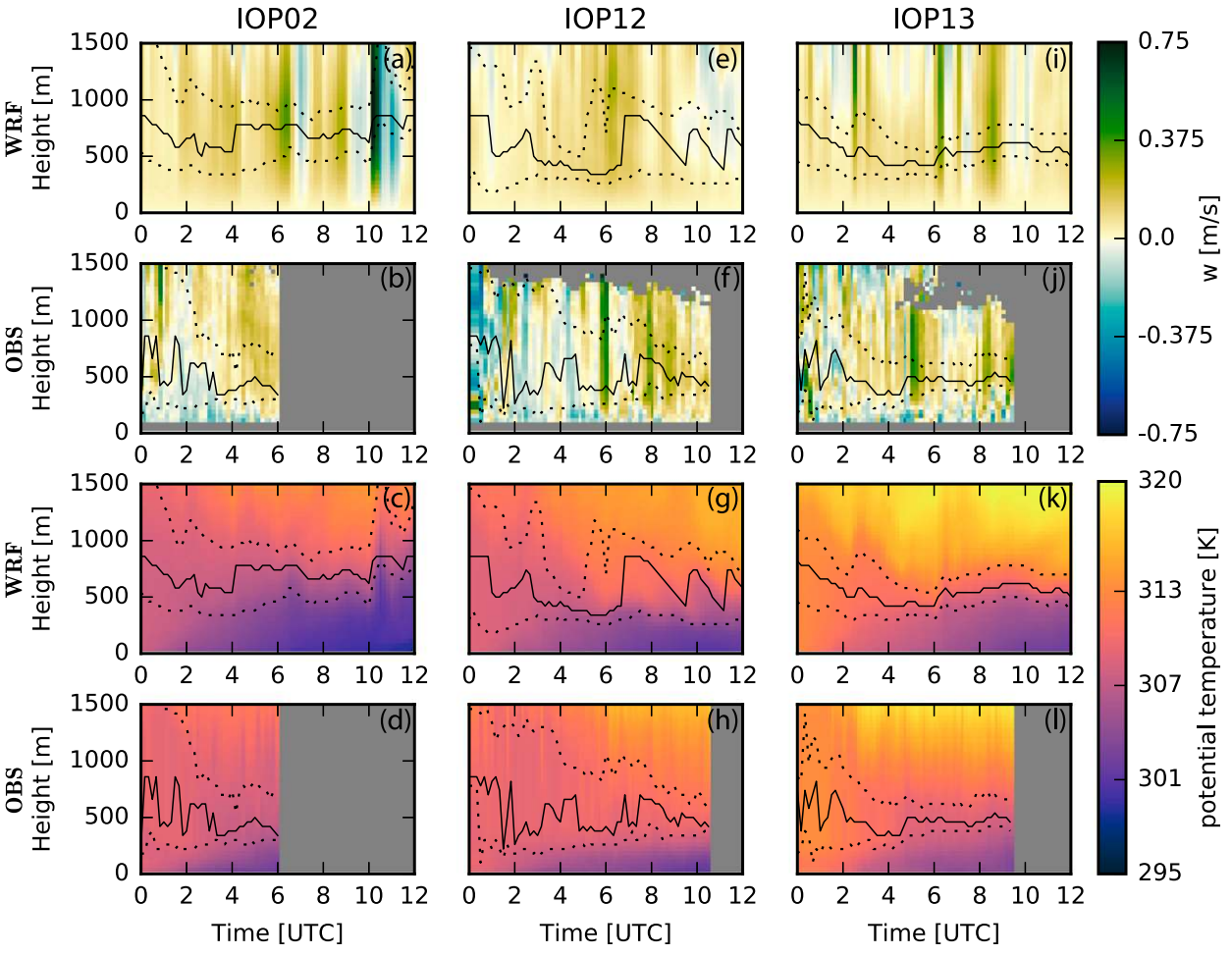

FIG. 6. Observed and simulated vertical velocity and potential temperature are shown at MP1 for IOP02, IOP12, and IOP13. Gray areas indicate observations are unavailable or omitted for quality purposes. Solid lines indicate the height of the NLLJ maximum, and the dotted lines encompass the core region, where the wind speed is at least 90% of the NLLJ maximum. For reference, sunset occurred near 0200 UTC (2100 CDT) and sunrise occurred shortly after 1100 UTC (0600 CDT). MP1 observations are available in Turner (2016d,b).

in addition to the cases explored in Smith et al. (2018), we feel confident that the three-dimensional simulated data are appropriate for further analysis designed to complement interpretations of the observations.

Plan-view wind speed and water vapor mixing ratio fields at 500 m AGL (near the height of the NLLJ maximum) are shown in Figs. 9 and 10. Moisture is shown as a pseudopassive tracer of the flow. At 0000 UTC (Figs. 9a, 10a), the NLLJ had not yet formed and the 500 m winds were out of the south-southeast. A swath of moisture was situated over most of Kansas with the highest moisture content located on the Kansas–Oklahoma border southwest of FP2. By 0300 UTC (Figs. 9b, 10b), wind speed increased—especially in the western parts of Kansas and Oklahoma, and winds were more southerly. Moisture was still in place, with an area of increased moisture content stretched farther north from west of FP2 to northwest of FP3, implying southerly advection had occurred. At 0600 UTC (Figs. 9c, 10c), wind speed had continued to increase especially in western Kansas and Oklahoma. Wind vectors began to turn indicating the 500-m wind was veering (changing direction in a clockwise fashion) at Hays and locations west of it. The eastern parts of Kansas and Oklahoma were still characterized by weaker winds from the south. The veering winds began to push the moisture swath toward the east, advecting drier air into place from the west. Finally, at 0900 UTC (Figs. 9d, 10d) the wind vectors had a westerly component across the entirety of Kansas and Oklahoma. Winds were still weaker in the eastern portion of the domain. The moisture swath was now located over the eastern portion of Kansas as drier air occupied west Kansas, where winds were more westerly indicating westerly advection had become

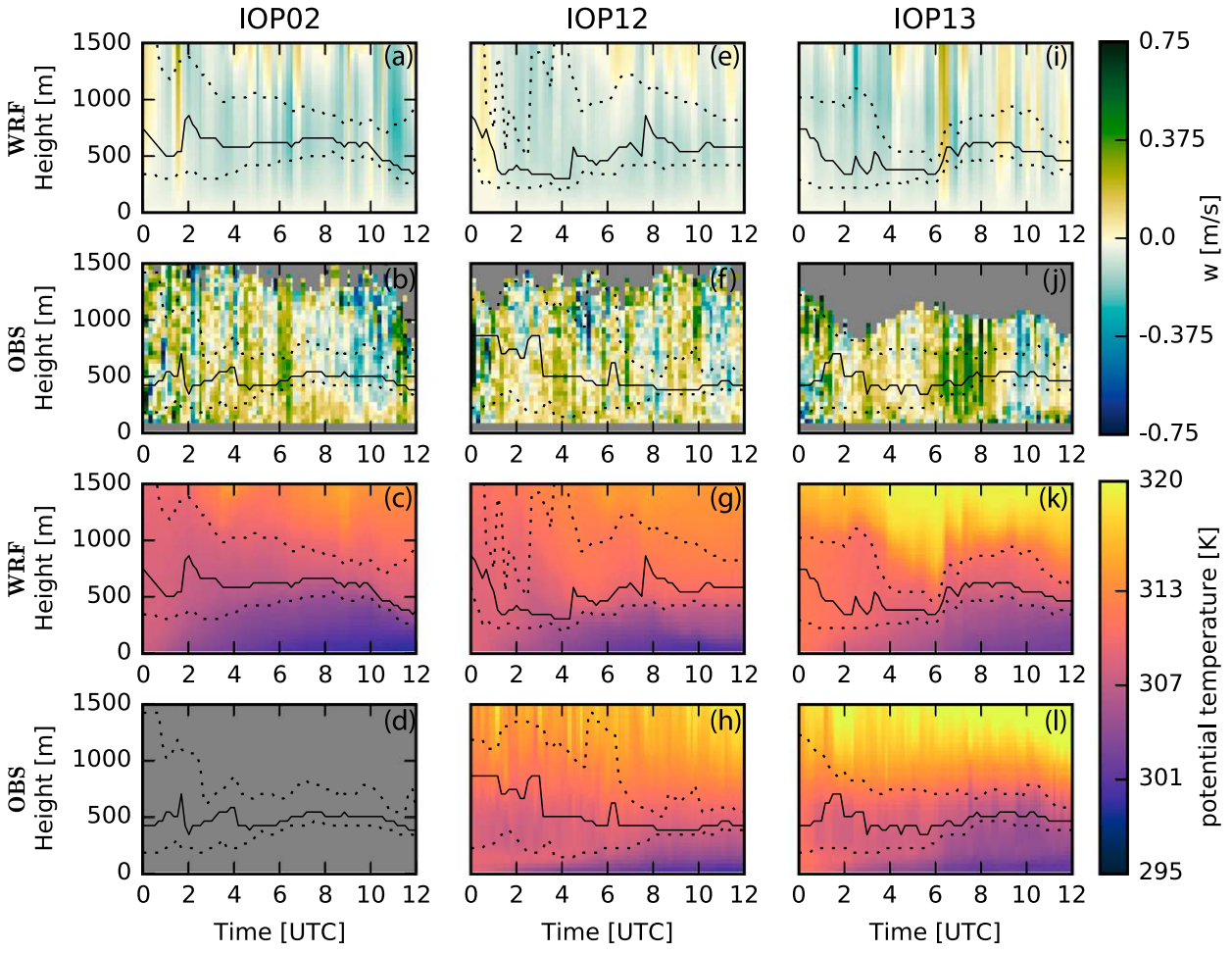

FIG. 7. As in Fig. 6, but for site FP2. For reference, sunset occurred near 0200 UTC (2100 CDT) and sunrise occurred shortly after 1100 UTC (0600 CDT). The AERI was not yet fully operational at FP2 during IOP02. FP2 observations are available in Turner (2016a).

significant overnight. This evolution suggests that the NLLJ was moving across the Great Plains, and advection was prominent along the slope instead of just from the south during the night. The presented analysis, however, does not offer any information about how the vertical structure of the NLLJ evolved through the night.

To track the evolution of the structure of the NLLJ, vertical cross sections were taken from WRF simulation data across the slope of the Great Plains at about 39.55°N near the Kansas–Nebraska border (Fig. 11). At 0000 UTC (Fig. 11a), isentropes were nearly vertical indicating a well-mixed boundary layer. The moisture field was bounded within this well-mixed boundary layer, which was deeper over the western portion of the slope as compared with the eastern portion. Except for regions near the surface and outside the boundary layer, winds were already mostly southerly, with some locally stronger winds over the western most portion of the slope. By 0300 UTC (Fig. 11b) the SBL formed near the surface. Wind speeds increased within the NLLJ, with the area of strongest winds located west of 99°W. In the western most portion of the cross section, the wind direction had already begun to veer near the top of the NLLJ as it acquired an increased westerly component. This westerly component began to transport the moisture field from west to east above the slope. As suggested by the plan-view analysis (see Figs. 9 and 10), by 0600 UTC (Fig. 11c) stability and the NLLJ strengthened and the elevated region with stronger winds reached farther east. Moisture advected east, which deepened the moist layer over the eastern region and reduced moisture in the west. Winds were weaker and mostly southerly over the easternmost portion of the domain. Winds had veered vertically throughout the NLLJ west of 99°W. Just east of 99°W, the veering of NLLJ winds with height was apparent near the top of the NLLJ, but not yet in the core or near the surface.

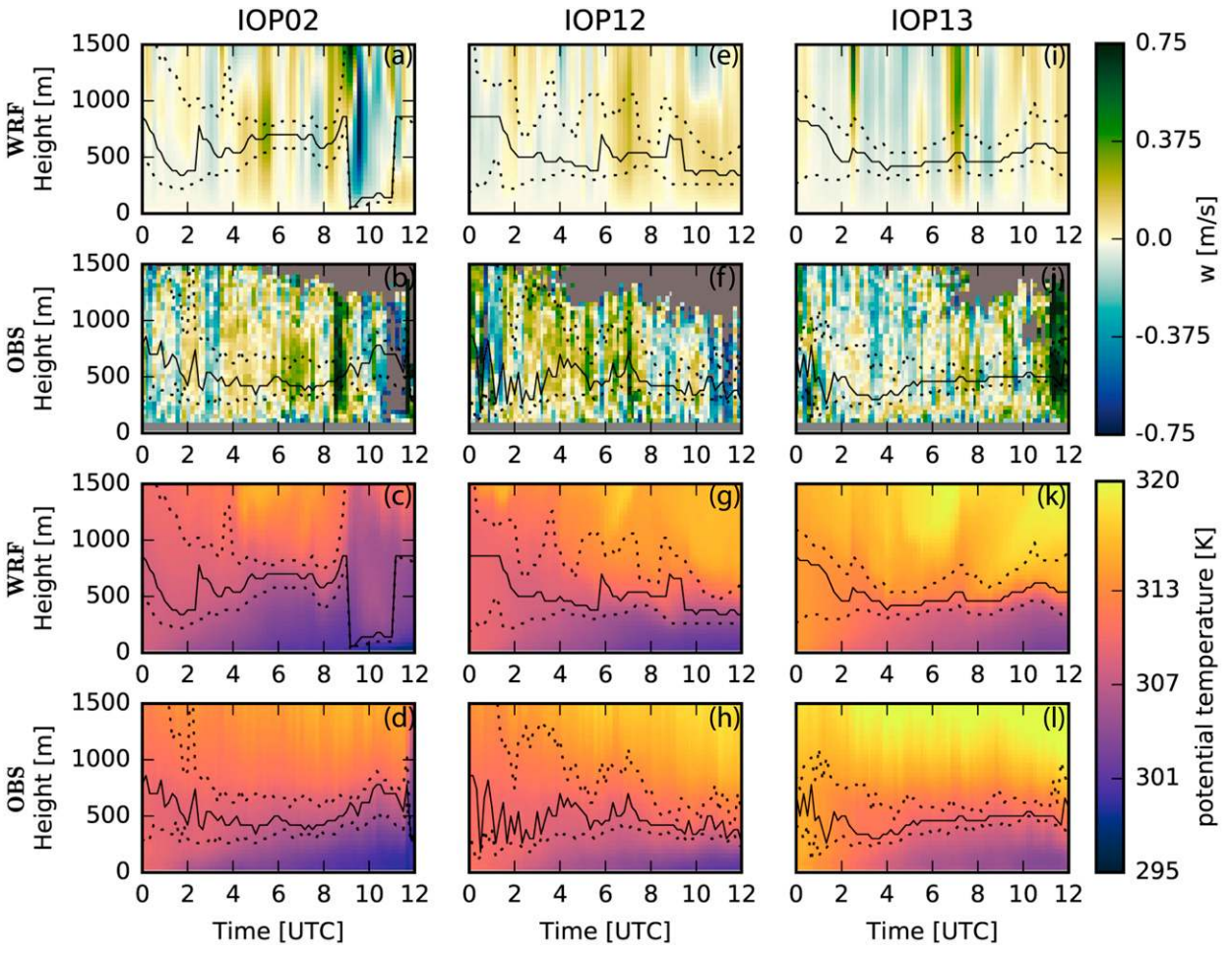

FIG. 8. As in Fig. 6, but for site FP3. For reference, sunset occurred near 0200 UTC (2100 CDT) and sunrise occurred shortly after 1100 UTC (0600 CDT). FP3 observations are available in Turner (2015).

Finally, at 0900 UTC (Fig. 11d) stability in the boundary layer generally continued to increase as the surface cooled and higher potential temperature advected farther east above the NLLJ. By this time, the moisture field was drastically different than how it looked early in the night, with a deep layer of moisture in the east and a very shallow moisture layer in the west. The region of strongest NLLJ winds was also farther east at this point, and the increasing westerly component led to south-southwesterly winds across the entire area.

Previously, vertical motions like those observed and simulated during PECAN cases have usually been explained by convergence at the eastern edge or at the terminus of the NLLJ (e.g., Bonner 1966). The NLLJ has been known to veer with time due to the inertial oscillation (Blackadar 1957). The associated change of wind direction causes convergent regions within the NLLJ to evolve in time (Bonner 1966). More recently, Walters and Winkler (2001) showed that half of NLLJs observed over the Great Plains do veer with height. Veering in time and height means that the cross-jet component (the u component in the Great Plains) becomes important, and the nonlinear advection terms in the equations of motion can result in eastward down-slope advection of the NLLJ by the NLLJ itself (Fedorovich et al. 2017; Gebauer et al. 2018). Paegle and Rasch (1973) suggested that the nonlinear terms can create vertical motions within the horizontally heterogeneous NLLJ.

The NLLJ from IOP12 is a clear example of NLLJ evolution along the sloping terrain of the Great Plains as shown in Fig. 11. This dynamic evolution of the NLLJ has not been well documented in the literature. Comparing the 0000 UTC panel (Fig. 11a) with the 0900 UTC panel (Fig. 11d) makes clear the down-slope propagation of the core region of the NLLJ. It is proposed that veering of wind with height causes differential

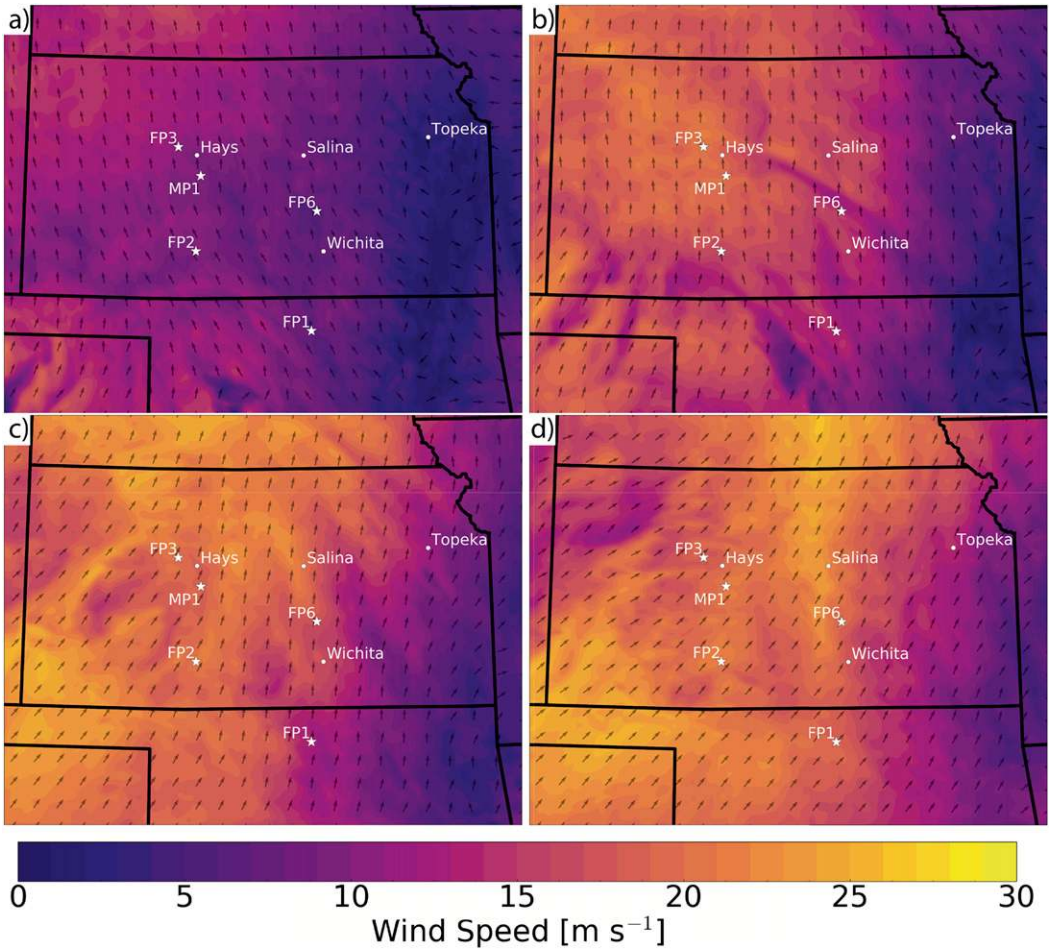

FIG. 9. Plan views of the NLLJ at 500 m AGL are shown for IOP12 WRF simulation at (a) 0000 UTC, (b) 0300 UTC, (c) 0600 UTC, and (d) 0900 UTC. Arrows denote wind direction while the colorfill shows the wind speed. For reference, sunset occurred near 0200 UTC (2100 CDT) and sunrise occurred shortly after 1100 UTC (0600 CDT).

down-slope advection of the NLLJ. In other words, the NLLJ moves from west to east down the slope. The increased westerly wind component (the *u* component) at the top of the NLLJ combined with NLLJ heterogeneity (e.g., nonuniform NLLJ height, wind speed, and wind direction along the slope) results in local regions conducive to convergence at the top eastern edge of the NLLJ, which is favorable for the development of local updrafts. Profiles of the *u* component of velocity in Fig. 12 show that the *u* maximum is first located at or above 1000 m and descends through the night, but the maximum descends much earlier in the western profiles. In Fig. 11 a local region of convergence and associated vertical motion can be seen at 0600 UTC just east of 99°W, where higher wind speeds with slightly more westerly direction west of this point meet slower, more southerly winds. Note that an updraft feature was simulated and observed at MP1 and FP3 at about this time. This mechanism is proposed as a possible source of the vertical motions observed and simulated with the WRF Model for PECAN cases. It is also a possible driver of nocturnal convection initiation over the Great Plains (Gebauer et al. 2018).

Diagonal striations are an observed signature that can reveal NLLJ spatial evolution from a single point observation. These signatures have been documented before (Gebauer et al. 2018), but not thoroughly explained. The veering of NLLJ winds in height and in time as well as the jet's downslope advection explains the diagonal striation signatures seen in time–height cross sections of wind speed. As illustrated in Fig. 13, NLLJ wind speed increases and wind direction veers first at the top of the NLLJ, then deepens from the top down. In point observations (Fig. 13d), the differential advection of the stronger winds to the west manifests as a diagonal striation signature. In the PECAN

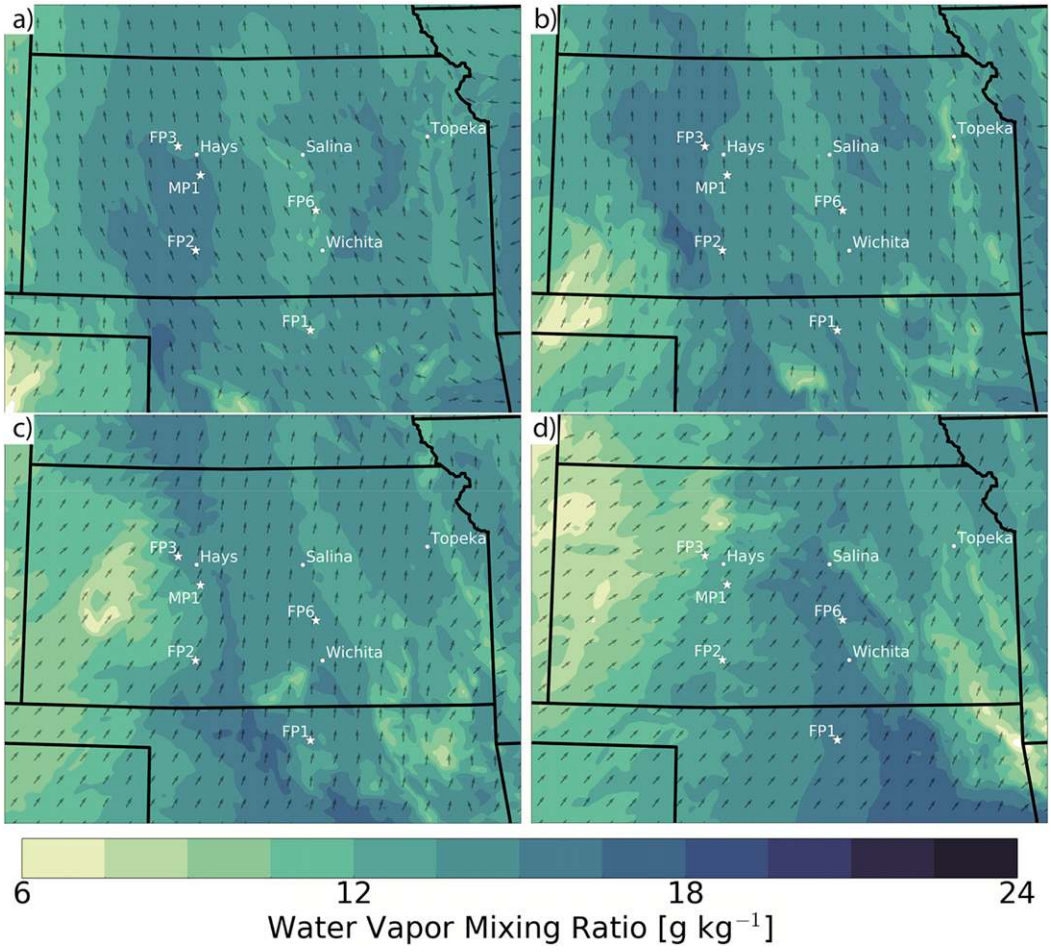

FIG. 10. As in Fig. 9, but the colorfill shows water vapor mixing ratio. For reference, sunset occurred near 0200 UTC (2100 CDT) and sunrise occurred shortly after 1100 UTC (0600 CDT).

observations, diagonal striation signatures in in the wind speed fields coincided with an increased westerly component of the wind. This same process causes the warming in the region above the NLLJ. As the westerly wind component increases, higher potential temperature is advected down the slope. This advection is evident in the profiles shown in Fig. 12, where the trends in the moisture and potential temperature profiles can be connected to maxima in the u profile.

The newly identified and described spatiotemporal evolution of the NLLJ results in temporal NLLJ evolution appearing differently at different locations on the slope. Time–height cross sections of WRF Model results similar to those shown in the previous section are presented in Fig. 14 at FP3, FP2, FP6, and FP1 (see Fig. 1 for locations) to illustrate the evolution of simulated local NLLJ features across the PECAN domain. At the western sites (FP3, FP2), the NLLJ depth and magnitude were greater compared to the eastern sites (FP6, FP1). At all four sites, some diagonal striation features appeared in the wind speed field. A sudden instance of upward vertical motion was simulated at FP3 at about 0700 UTC, while no such rising motion occurred to the south at FP2. To the east at FP6, a similar but shorter duration vertical motion was simulated shortly after 0800 UTC; however, the southern site, FP1, did not show one. Diagonal striation signatures are thus not always precursors for vertical motion, but do suggest spatial NLLJ heterogeneity. The northern sites, FP3 and FP6, showed more drastic examples of these diagonal striation signatures. The first diagonal striation at FP3 began at about 0600 UTC near 1000 m AGL and reached 500 m AGL by 0700 UTC. This signature coincided with the updraft simulated at FP3. The diagonal striation at FP6 began later, at about 0800 UTC, near 1000 m AGL and reached 500 m AGL by 1000 UTC. Again, this signature was coincident with the updraft simulated at FP6. At all sites,

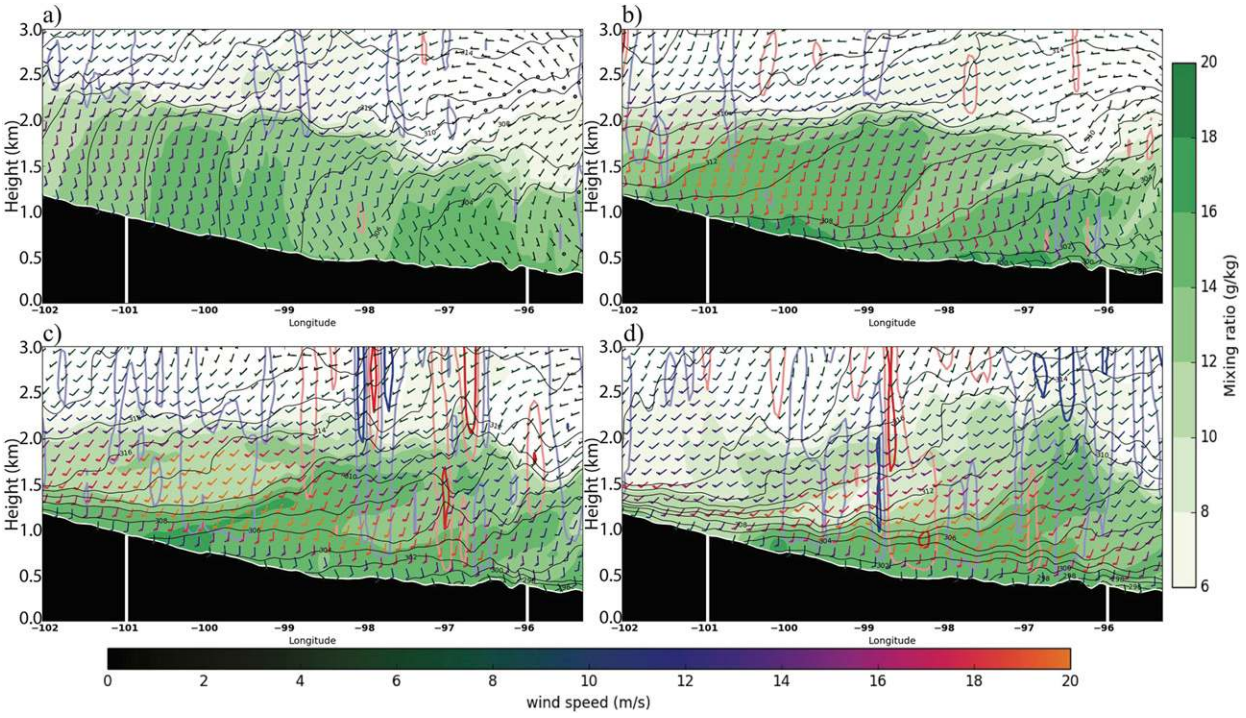

FIG. 11. Vertical cross sections were taken along latitude 39.55°N near the Kansas–Nebraska border from the IOP12 WRF simulation. The panels show potential temperature (K, black contours), wind speed (m s^{-1}, colored barbs), vertical velocity (m s^{-1}, colored contours where blue/red denotes downward/upward motion), and water vapor mixing ratio (>6 g kg^{-1}, green shading) at (a) 0000 UTC, (b) 0300 UTC, (c) 0600 UTC, and (d) 0900 UTC. The sloping terrain of the Great Plains is represented by the black region along the bottom of each panel. White lines over the terrain mark locations of profiles shown in Fig. 12. For reference, sunset occurred near 0200 UTC (2100 CDT) and sunrise occurred shortly after 1100 UTC (0600 CDT).

the NLLJ veered with height and time, but differences exist in the timing based on sited longitude. The wind direction pattern shows that the diagonal striations in the wind speed at each site coincided with increased westerly component of the wind. Related to sunset time, the SBL formed at similar times at all considered locations. However, the warming in the region above the NLLJ occurred later and was less pronounced at eastern sites (FP6 and FP1).

The previous discussion focused on IOP12 as an example of NLLJ heterogeneity and dynamic evolution. IOP02 and IOP13 will now be explored and compared to the example of IOP12. PECAN observations from IOP02 and IOP13 along the north–south transect are shown at FP3 in Figs. 4 and 8, at MP1 in Figs. 2 and 6, and at FP2 in Figs. 3 and 7. Both cases showed the NLLJ forming during the evening transition and remaining at or near 500 m AGL through the night. As in IOP12, both IOP02 and IOP13 NLLJs veered toward the south-southwest with time and height. Compared to IOP12, neither case showed such prominent diagonal striation signatures, but similar changes to NLLJ height, depth, and structure were observed along with sudden vertical motions. Along-slope cross sections for IOP02 and IOP13 are shown in Figs. 15 and 16, respectively. In general, the simulated motion fields in both cases are more chaotic than IOP12. This makes relating vertical motion to heterogeneity and local zones of convergence difficult. The NLLJ during IOP02 is somewhat less heterogeneous than IOP12, but more heterogeneous than the NLLJ that formed during warm conditions associated with synoptic ridging during IOP13. However, basic features of the identified NLLJ spatiotemporal evolution are apparent in each case including NLLJ motion down the slope, top-down increase in westerly winds, and associated moisture transport and warm air advection above the NLLJ.

So far, this study has documented and described temporal–spatial evolution of the NLLJ over the Great Plains in detail. Utilizing the mesoscale model (i.e., the WRF Model) was critical for the analysis of these spatiotemporal characteristics. On the other hand, the chosen approach of running simulations with 4-km spaced grids using PBL parameterization is not ideal for diagnosing turbulence and stability parameters

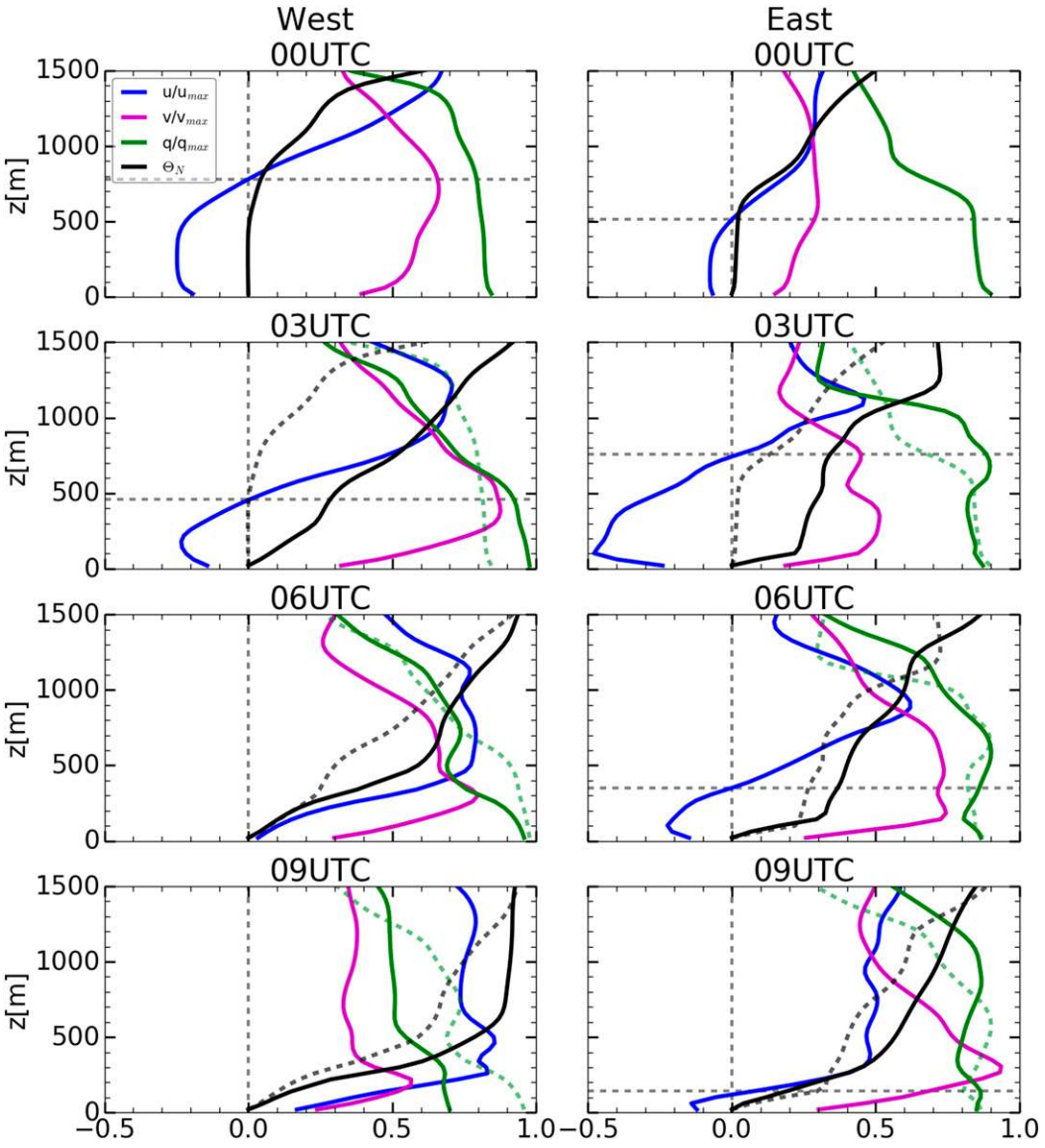

FIG. 12. Profiles on the west (101°W) and east (96°W) portion of the slope at 39.55°N are shown for u, v, q (all normalized by their respective overnight maxima), and θ_N (the deviation of θ from its surface value normalized by the overnight maximum deviation). For 0300–0900 UTC the previous time's θ and θ_N profile is shown by the dashed green and black lines, respectively. Dashed gray lines show the zero profile and the height at which u becomes zero where applicable. The locations where the profiles are taken are shown by white lines in Fig. 11. For reference, sunset occurred near 0200 UTC (2100 CDT) and sunrise occurred shortly after 1100 UTC (0600 CDT).

(e.g., turbulent diffusivity, TKE, Richardson number, etc.) in the boundary layer. This means that the effect of spatiotemporal variations of turbulent mixing on NLLJ evolution could not be further investigated using the mesoscale model output. Based on results described in Shapiro et al. (2016), which showed that interactions between the inertial oscillation mechanism [as described by Blackadar (1957)] and the buoyancy mechanism [diurnal heating and cooling of a sloped surface as described by Holton (1967)] play an important role, we hypothesize that variations in buoyancy may be an important mechanism contributing to the pronounced spatiotemporal evolution of the NLLJ, and these effects can be investigated using the mesoscale model output. A brief and general discussion will now be offered to demonstrate buoyancy's potential role in forcing dynamic behavior of the NLLJ over the Great Plains.

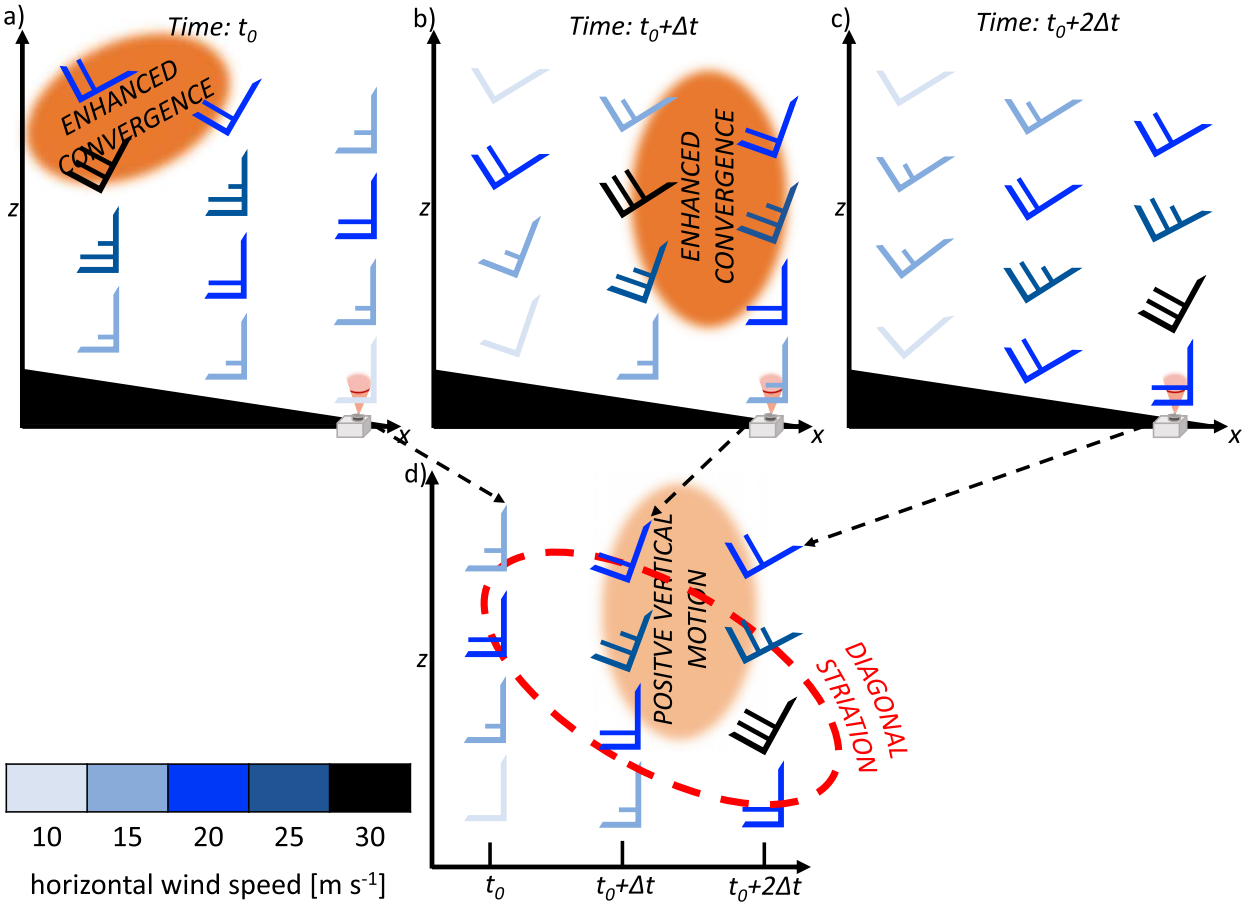

FIG. 13. (a)–(c) Conceptual diagram of the evolution of the heterogeneous NLLJ across the slope and (d) the resulting profile observation.

A one-dimensional model for NLLJ dynamics was initially proposed in Shapiro et al. (2016) (and later summarized in Gebauer et al. 2017) based on the Boussinesq equations of motion and thermal energy in slope-following coordinates (see Fig. 17). Only the most relevant equations for our discussion are reproduced here (see the full model framework in Shapiro et al. 2016). In the case of an eastward-facing slope with slope angle $\alpha > 0$, the east–west equation of motion can be written as

$$\frac{\partial u}{\partial t} = -fV_g + fv + K\frac{\partial^2 u}{\partial z^2}, \tag{1}$$

where the local PBL geostrophic wind is given by

$$V_g(z,t) = v_{g_\infty} + \frac{1}{f} b \sin\alpha, \tag{2}$$

the sum of the constant free atmosphere geostrophic wind $[v_{g_\infty} = 1/f(\partial\Pi/\partial x)_\infty]$ and the contribution from buoyancy along the sloped surface. The x and y components of the wind are represented by u and v, respectively. Buoyancy is represented by b, and Π is the normalized pressure perturbation. The Coriolis parameter is shown as $f \equiv 2\Omega \cdot \hat{\mathbf{k}}$, where Ω is the angular velocity of Earth's rotation and $\hat{\mathbf{k}}$ is the z-direction unit vector; K denotes the eddy diffusivity, treated here as height independent and equal for momentum and heat. Since buoyancy can vary in time and height, the PBL geostrophic wind, V_g must also vary in time and height. In the present work, this one-dimensional model is used as a theoretical framework for understanding NLLJ dynamics.

Buoyancy can be defined as

$$b = \frac{g}{\theta_0}\left[\theta_v - \theta_{v_r}(z)\right], \tag{3}$$

where g is the gravitational acceleration, θ_0 is a constant reference potential temperature, θ_v is the virtual potential temperature, and $\theta_{v_r}(z)$ is a reference profile

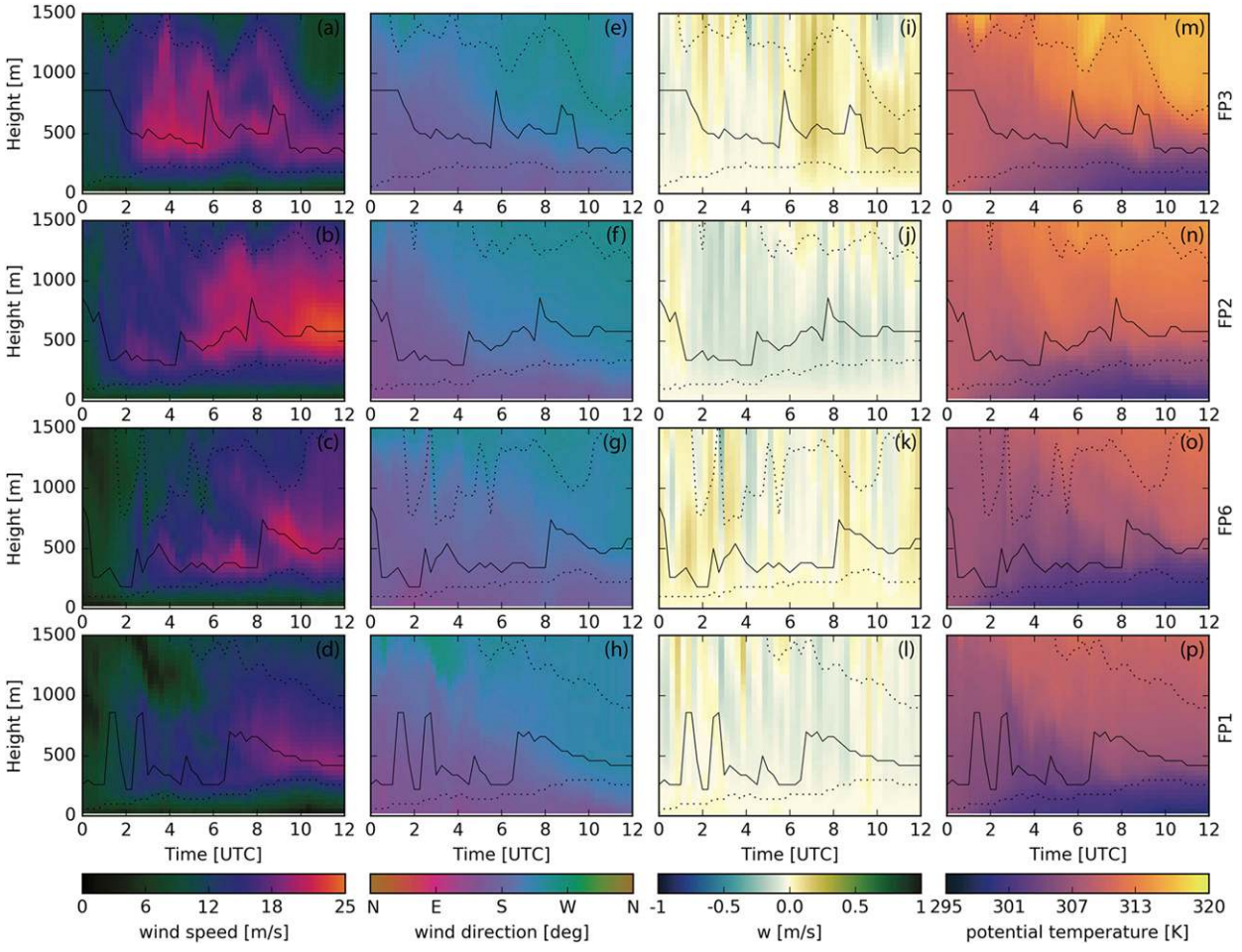

FIG. 14. Time–height cross sections of WRF simulated (a)–(d) wind speed, (e)–(h) wind direction, (i)–(l) vertical velocity, and (m)–(p) potential temperature are shown during IOP12 at four sites: (a),(e),(i),(m) FP3, (b),(f),(j),(n) FP2, (c),(g),(k),(o) FP6, and (d),(h),(l),(p) FP1. Solid lines indicate the height of the NLLJ maximum, and the dotted lines encompass the core region, where the wind speed is at least 90% of the NLLJ maximum. For reference, sunset occurred near 0200 UTC (2100 CDT) and sunrise occurred shortly after 1100 UTC (0600 CDT).

of virtual potential temperature (also known as the environmental potential temperature). In this application, we find $\theta_{v_r}(z)$ by taking the average free atmosphere θ_v along the slope and the environmental lapse rate, $\partial\theta_{v_r}/\partial z$, that satisfies a prescribed Brunt–Väisälä frequency [$N = \sqrt{(g/\theta_0)(\partial\theta_{v_r}/\partial z)}$] of 0.01. Buoyancy is an important component to NLLJ dynamics over the Great Plains because the Great Plains are sloped, leading to the tilted coordinate system shown in Fig. 17. Buoyant accelerations act along the true vertical direction z^*, but in tilted coordinates buoyant accelerations have components along the slope-normal z and along-slope x directions. In the presence of an eastward-facing slope like that of the Great Plains, two new buoyancy related drivers of NLLJ evolution can be described.

First, differential PBL geostrophic wind V_g, due to gradients of buoyancy along the slope, can be connected to observed and simulated NLLJ features. In the three PECAN cases discussed above, observations and simulations showed deeper boundary layers over the western portion of the slope. Warmer conditions through the boundary layer depth allow buoyancy [defined in Eq. (3)] to reach larger magnitudes over the western portion of the slope compared to the east leading to negative buoyancy gradients along the slope. Larger buoyancy magnitudes in the west contribute to greater values of PBL geostrophic wind V_g in Eq. (2). Stronger V_g in the west leads to a stronger inertial oscillation as described by Blackadar (1957), and thus a stronger NLLJ maximum in the west. The NLLJ has been known to veer with time due to the inertial oscillation (Blackadar 1957). The associated change of wind direction combined with the differential V_g can cause broad

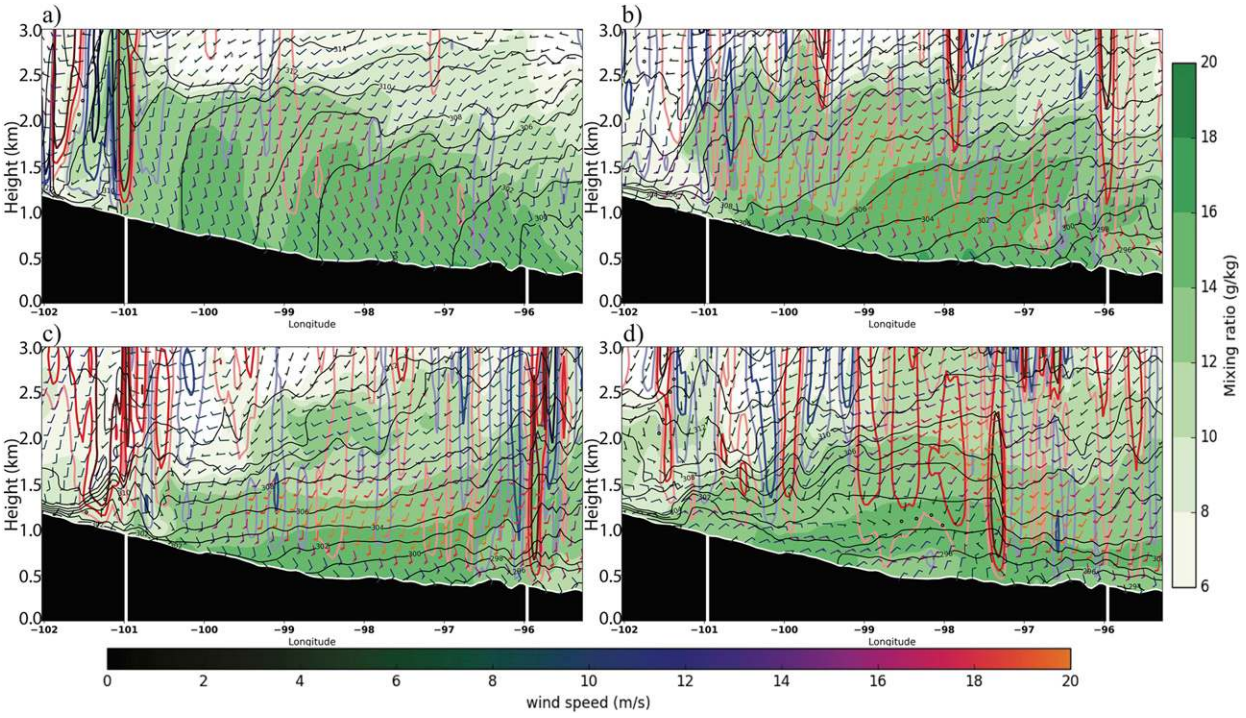

FIG. 15. As in Fig. 11, but for IOP02. For reference, sunset occurred near 0200 UTC (2100 CDT) and sunrise occurred shortly after 1100 UTC (0600 CDT).

convergent regions within the NLLJ to evolve in time (Bonner 1966).

Second, temporal evolution of the u component of velocity due to temporal buoyancy evolution can be connected to observed and simulated east–west motion of the NLLJ. The time tendency of the u component of velocity on an eastward-facing slope is described in Eq. (1). The first terms on the right-hand side is described in Eq. (2) as the PBL geostrophic wind. For $\partial u/\partial t$ to be nonzero, V_g must change, assuming that eddy diffusivity K is constant and we consider time scales short enough to disregard turning of the v component by the Coriolis force. If background conditions are quiescent, changes in v_{g_∞} should remain small enough to neglect, meaning any change in V_g would be due to change in b. Moreover, if b changes at different rates at different locations along the slope, $\partial u/\partial t$ would evolve differently at different locations, which could lead to nonlinear momentum advection by the u component [i.e., $u(\partial u/\partial x)$] and enhanced local convergence regions since the u component of velocity could become stronger in the west than in the east.

To evaluate evolution of the NBL and NLLJ through the night buoyancy gradients were computed between a west (36.5° latitude, −100° longitude) and east (36.5° latitude, −95° longitude) site. Perturbation profiles were constructed at the same sites. This method defined a perturbation as a deviation from the overnight mean state. These perturbation profiles are computed for virtual potential temperature θ_v and the u component of velocity. Perturbations of θ_v are used in lieu of buoyancy since magnitude of the reference state and constants are removed in the computation of the perturbation ($b' = \theta_v'$), and perturbations to the temperature field are more tangible than buoyancy. Buoyancy gradients are shown in Fig. 18 while θ_v' and u' profiles are shown in Figs. 19 and 20, respectively.

The buoyancy gradients and both sets of perturbation profiles were generally similar for IOPs 02 and 12, but less similar for IOP13. This is consistent with the case descriptions above where IOPs 02 and 12 appeared more similar while IOP13 was the strongest NLLJ, with the most uniform winds across the domain, and occurred after the warmest daytime PBL. For all cases, the buoyancy gradient remained negative throughout most of the night, indicating that differential PBL geostrophic wind, V_g could have led to stronger NLLJ magnitudes in the west.

The buoyancy gradient in IOP13 evolved less rapidly than in IOPs 02 and 12. This slower evolution could lead to a less drastic temporal evolution of the u component of velocity, or in other words, the first buoyancy related driver discussed above would have dominated NLLJ evolution. Figures 19 and 20 confirm that temporal

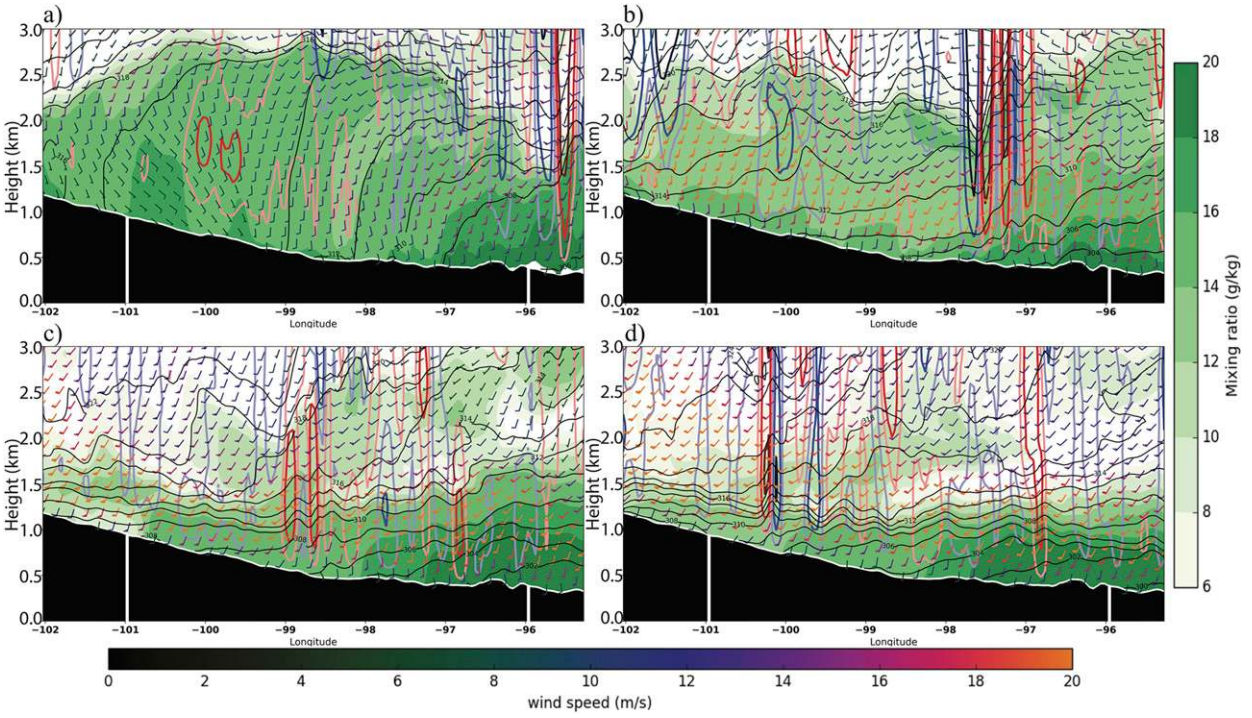

FIG. 16. As in Fig. 11, but for IOP13. For reference, sunset occurred near 0200 UTC (2100 CDT) and sunrise occurred shortly after 1100 UTC (0600 CDT).

evolution is different at the two profile sites for IOPs 02 and 12, but similar for IOP13. Synoptic conditions were dominated by broader zonal flow during IOP13, which allowed the eastern edge of the NLLJ to be much farther east than in IOPs 02 and 12 resulting in a broader NLLJ. Since the preceding daytime PBL was so much warmer in IOP13, we hypothesize that the eastern site behaves much more similarly to the western site under conditions like those in IOP02 and IOP12.

For IOPs 02 and 12, temporal evolution of the u component of velocity due to temporal buoyancy evolution can be connected to observed and simulated east–west motion of the NLLJ. In Fig. 19, it is apparent that the overnight cycle of virtual potential temperature near the surface is larger in the west. Strongly positive perturbations early in the night give way to strongly negative perturbations late in the night below 500 m AGL. A similar pattern (positive to negative perturbation) is apparent at the eastern site, but the magnitude of the cycle is smaller, and it takes longer for the perturbation to become negative. The pattern reverses in the layer above 500 m AGL. Perturbation profiles for the u component of velocity in Fig. 20 can be related to the evolution of composite perturbation profiles for θ_v in Fig. 19 (and thus b). In the layer between 250 and 750 m at the west site for clear cases, u' profiles show the most pronounced overnight cycle from strongly negative, to strongly positive. The same pattern, though less drastic, is evident in the same layer at the east site for similar cases. As the u component of velocity strengthens in the layer above 250 m AGL, downslope winds increase buoyancy through downslope advection of environmental potential temperature, leading to the more dramatic changes of θ_v' profiles at the west site. At the east site, the cycle in u' profiles is generally less pronounced, and occurs over a deeper layer. Since θ_v (and therefore b) changes more rapidly in the west, V_g must change more rapidly, forcing $\partial u/\partial t$ to be greater in the west than in the east.

It is important to note that a gradient in buoyancy should lead to the generation of positive y-component vorticity as required by the y-component vorticity equation [see Markowski and Richardson (2010), their Eq. (2.94)]. A negative buoyancy gradient leads to a positive contribution to the time rate of change of y-component vorticity η. Since $\eta = [(\partial u/\partial z) - (\partial w/\partial x)]$, we can expect that a positive rate of change of η can then lead to an increase in $\partial u/\partial z$, and the u component of velocity can be enhanced with height. This effect can explain why the upper portion of the NLLJ develops the stronger u components, why the top portion of the NLLJ is advected downslope earlier in the night, and why

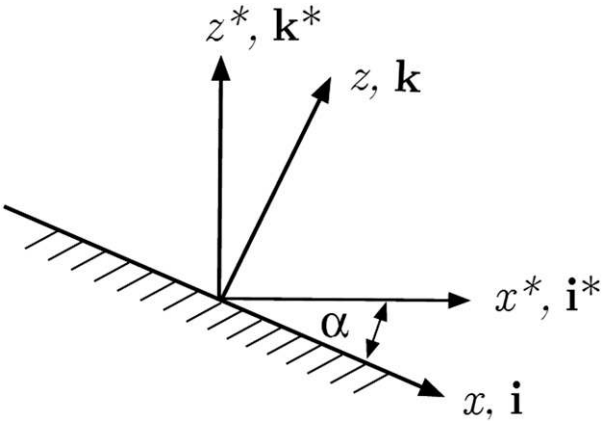

FIG. 17. The slope following coordinate system used in the one-dimensional model of NLLJ dynamics proposed by Shapiro et al. (2016) (adapted from their Fig. 1).

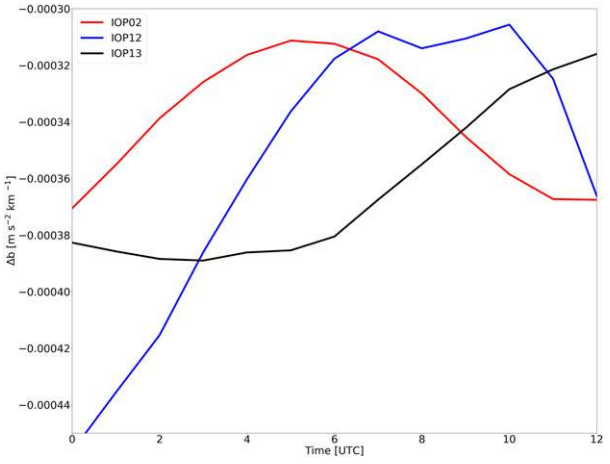

FIG. 18. Simulated buoyancy gradients between the west (36.5° latitude, −100° longitude) and east (36.5° latitude, −95° longitude) profile locations for PECAN IOPs 02, 12, and 13. For reference, sunset occurred near 0200 UTC (2100 CDT) and sunrise occurred shortly after 1100 UTC (0600 CDT).

warmer potential temperatures are advected from west to east above the NLLJ.

6. Summary and conclusions

The PECAN field campaign provided unprecedented high-resolution observational datasets including several NLLJ cases. Using these data in conjunction with optimally configured WRF Model simulations offered a robust dataset for analyses of the NLLJ and the atmospheric boundary layer in which it forms. Profile observations from PECAN sites along a north–south transect, MP1, FP2, and FP3, were used to further evaluate the WRF Model configuration introduced in Smith et al. (2018). Analyses concluded that the simulated NLLJs formed earlier than the observed NLLJs. These simulated NLLJs were too strong early in the night and too weak later in the night as compared with observations. Nevertheless, the WRF Model successfully represented the general structure and evolution of the observed NLLJs, and it was able to reproduce sudden variations in boundary layer winds such as the diagonal striations observed during IOP12. The height of the NLLJ maximum and the core region of the jet were also well represented by the WRF Model. Simulated potential temperature fields closely matched observations, as they successfully captured the simultaneous surface layer cooling and warming above the NLLJ maximum. Finally, the WRF Model produced bursts of vertical motion resembling the updrafts that were observed at several sites during PECAN.

Overall, the WRF Model simulations were found to represent NLLJ features well. As such, the three-dimensional simulation data were used alongside PECAN observations to explore characteristics of the NLLJ over the Great Plains during PECAN. A summary of PECAN observations suggested that the spatial evolution of the NLLJ was responsible for sudden changes in the NLLJ structure manifested via diagonal striation signatures in the time–height wind profiles with coincident increases in westerly winds, rising motion, and warm advection above the NLLJ nose. Plan-view analyses of WRF modeled wind speed and water vapor mixing ratio showed that the NLLJ moved from west to east down the slope during the night and advection was prominent along the slope. This momentum advection by the NLLJ was associated with the increased westerly component as the NLLJ veered in time. Strong westerly components were found to advect warmer environmental potential temperature down the slope. Vertical cross sections across the slope of the Great Plains showed that NLLJ winds veered not only in time but also in height. The westerly component first increased at the top of the NLLJ and gradually descended. This veering in height and time together appeared as a diagonal striation signature in time–height cross sections of wind observed and simulated at each site. The spatial evolution of the NLLJ led to sudden changes in local NLLJ structure and mixing in the NBL. In idealized simulations, Fedorovich et al. (2017) showed similar effects. Heterogeneity of the NLLJ with respect to its depth, wind speed, and wind direction was identified as a potential source of localized convergence and associated vertical motions. With sufficient saturation, this mechanism could be important for nocturnal convection initiation as explained in Gebauer et al. (2018),

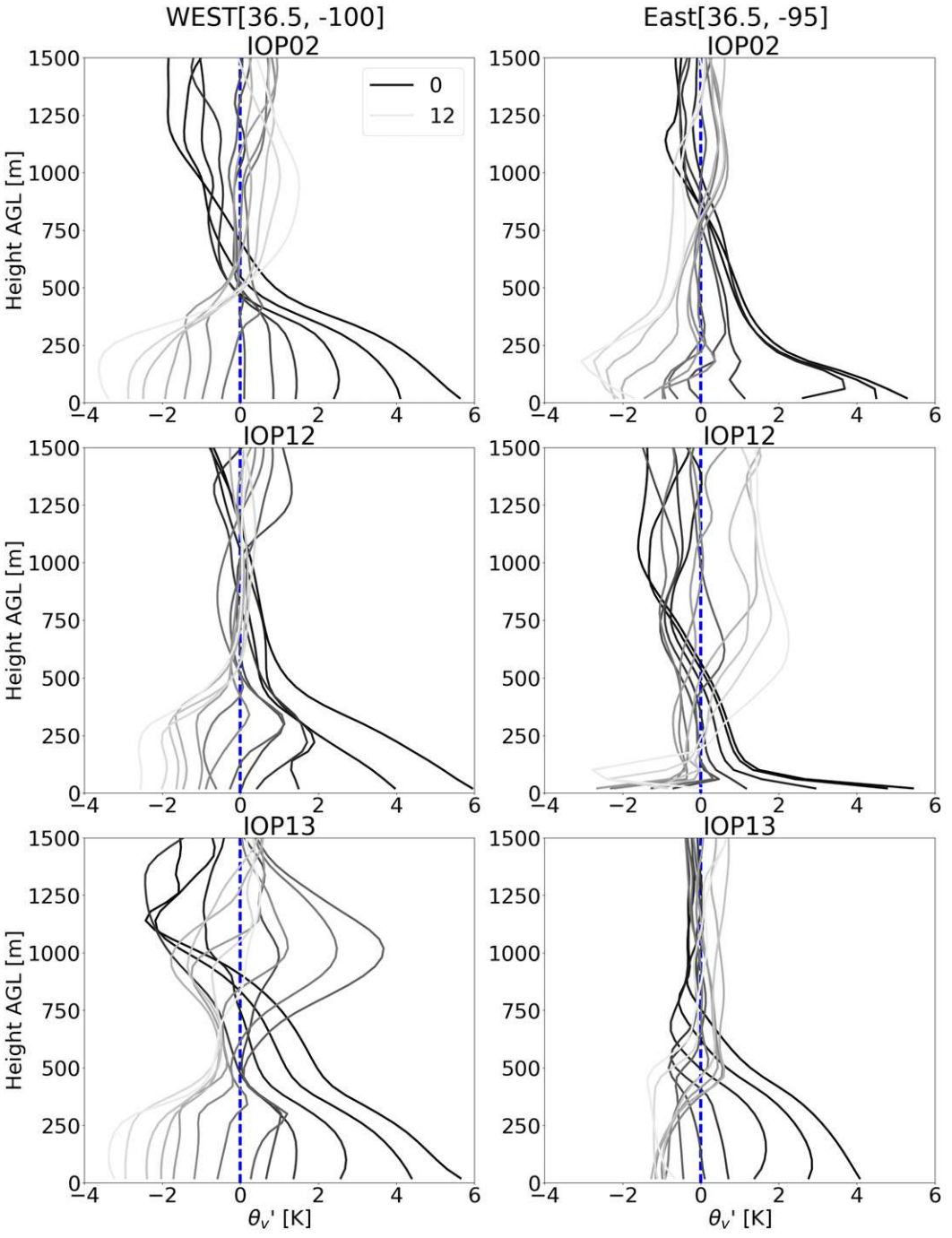

FIG. 19. Perturbation profiles of virtual potential temperature for PECAN IOPs 02, 12, and 13. Darker shades indicate earlier times during the night.

who found similar structures for additional PECAN cases.

This study demonstrated that the NLLJ is typically heterogeneous in depth, wind speed, and wind direction. Additionally, the heterogeneous NLLJ was shown to be moving across the slope of the Great Plains through the night. As such, the spatial and temporal characteristics of the NLLJ are deeply connected and should not be considered independently. Detailed description of these NLLJ features had not been documented in the literature. To explain the identified spatiotemporal NLLJ evolution, two new buoyancy drivers were identified:

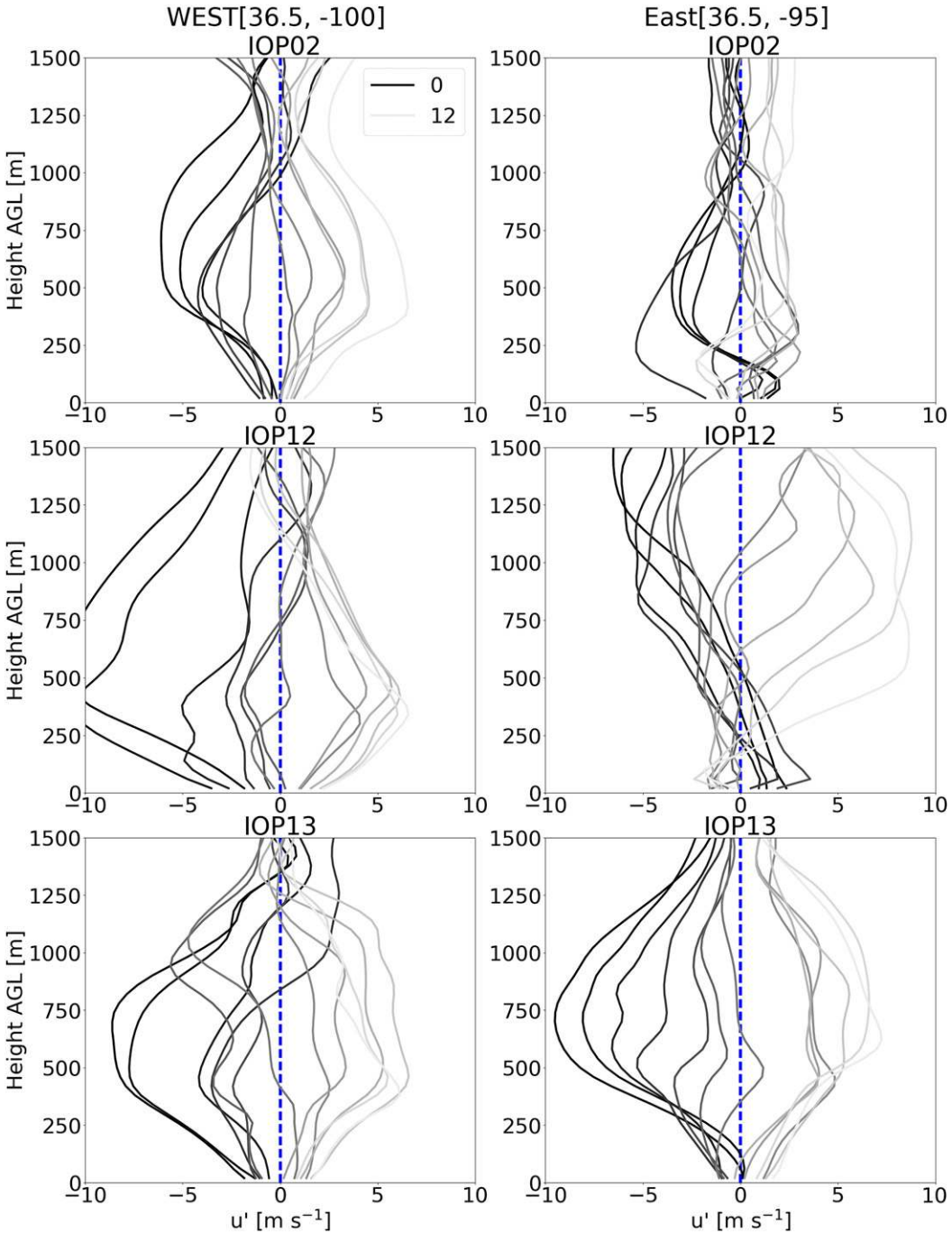

FIG. 20. As in Fig. 19, but for the *u* component of velocity.

differential PBL geostrophic wind and temporal evolution of the *u* component of velocity. The differential PBL geostrophic wind driver related deeper boundary layers in the western Great Plains to buoyancy gradients along the slope. Assuming background large-scale geostrophic wind is unchanged, higher magnitudes of buoyancy in the west result in stronger PBL geostrophic wind in that region. Based on inertial oscillation theory, stronger PBL geostrophic wind in the west leads to stronger NLLJ magnitudes in the west. The second buoyancy driver is forced by more rapid changes in buoyancy in the west compared to the east. As buoyancy changes more quickly, the time rate of change of the *u* component of velocity must change in response, leading

to enhanced turning of (already stronger due to the first driver) NLLJ winds in the western portion of the Great Plains. This enhanced veering can lead to heterogeneity in the NLLJ, locally strong convergence regions, and associated vertical motions. In a future study, we will investigate buoyancy gradients and the role of the described drivers in the Great Plains in more detail.

Acknowledgments. This research was supported by the National Science Foundation under Grant AGS-1359698. The authors wish to acknowledge the scientists involved in the PECAN data collection. The authors are grateful to Dr. Jacob Carlin of CIMMS and members of the OU-BLISS research group for their insights on this work. Dr. David Turner of NOAA assisted with data postprocessing. Brian Carroll of the University of Maryland, Baltimore County postprocessed lidar data for FP2.

REFERENCES

Ardanuy, P., 1979: On the observed diurnal oscillation of the Somali jet. *Mon. Wea. Rev.*, **107**, 1694–1700, https://doi.org/10.1175/1520-0493(1979)107<1694:OTODOO>2.0.CO;2.

Astling, E. G., J. Paegle, E. Miller, and C. J. O'Brien, 1985: Boundary layer control of nocturnal convection associated with a synoptic scale system. *Mon. Wea. Rev.*, **113**, 540–552, https://doi.org/10.1175/1520-0493(1985)113<0540:BLCONC>2.0.CO;2.

Baines, P., 1980: The dynamics of the Southerly Buster. *Aust. Meteor. Mag.*, **28** (4), 175–200.

Banta, R. M., 2008: Stable-boundary-layer regimes from the perspective of the low-level jet. *Acta Geophys.*, **56**, 58–87, https://doi.org/10.2478/s11600-007-0049-8.

——, R. Newsom, J. Lundquist, Y. Pichugina, R. Coulter, and L. Mahrt, 2002: Nocturnal low-level jet characteristics over Kansas during CASES-99. *Bound.-Layer Meteor.*, **105**, 221–252, https://doi.org/10.1023/A:1019992330866.

——, Y. L. Pichugina, and R. K. Newsom, 2003: Relationship between low-level jet properties and turbulence kinetic energy in the nocturnal stable boundary layer. *J. Atmos. Sci.*, **60**, 2549–2555, https://doi.org/10.1175/1520-0469(2003)060<2549:RBLJPA>2.0.CO;2.

——, ——, and W. A. Brewer, 2006: Turbulent velocity-variance profiles in the stable boundary layer generated by a nocturnal low-level jet. *J. Atmos. Sci.*, **63**, 2700–2719, https://doi.org/10.1175/JAS3776.1.

Blackadar, A. K., 1957: Boundary layer wind maxima and their significance for the growth of nocturnal inversions. *Bull. Amer. Meteor. Soc.*, **38**, 283–290, https://doi.org/10.1175/1520-0477-38.5.283.

Bonin, T. A., W. G. Blumberg, P. M. Klein, and P. B. Chilson, 2015: Thermodynamic and turbulence characteristics of the Southern Great Plains nocturnal boundary layer under differing turbulent regimes. *Bound.-Layer Meteor.*, **157**, 401–420, https://doi.org/10.1007/s10546-015-0072-2.

Bonner, W. D., 1966: Case study of thunderstorm activity in relation to the low-level jet. *Mon. Wea. Rev.*, **94**, 167–178, https://doi.org/10.1175/1520-0493(1966)094<0167:CSOTAI>2.3.CO;2.

——, 1968: Climatology of the low level jet. *Mon. Wea. Rev.*, **96**, 833–850, https://doi.org/10.1175/1520-0493(1968)096<0833:COTLLJ>2.0.CO;2.

Brook, R. R., 1985: The Koorin nocturnal low-level jet. *Bound.-Layer Meteor.*, **32**, 133–154, https://doi.org/10.1007/BF00120932.

Delgado, R., B. Carroll, and B. Demoz, 2015: FP2 UMBC Doppler lidar line of sight wind data, version 1.1. UCAR/NCAR, Earth Observing Laboratory, accessed 1 August 2017, doi:10.5065/d6q81b4h.

Fedorovich, E., J. A. Gibbs, and A. Shapiro, 2017: Numerical study of nocturnal low-level jets over gently sloping terrain. *J. Atmos. Sci.*, **74**, 2813–2834, https://doi.org/10.1175/JAS-D-17-0013.1.

Gebauer, J. G., E. Fedorovich, and A. Shapiro, 2017: A 1D theoretical analysis of northerly low-level jets over the Great Plains. *J. Atmos. Sci.*, **74**, 3419–3431, https://doi.org/10.1175/JAS-D-16-0333.1.

——, A. Shapiro, E. Fedorovich, and P. Klein, 2018: Convection initiation caused by heterogeneous low-level jets over the Great Plains. *Mon. Wea. Rev.*, **146**, 2615–2637, https://doi.org/10.1175/MWR-D-18-0002.1.

Geerts, B., and Coauthors, 2017: The 2015 Plains Elevated Convection At Night (PECAN) field project. *Bull. Amer. Meteor. Soc.*, **98**, 767–786, https://doi.org/10.1175/BAMS-D-15-00257.1.

Hanesiak, J., and D. Turner, 2016: FP3 University of Manitoba Doppler lidar wind profile data, version 1.0. UCAR/NCAR, Earth Observing Laboratory, accessed 1 August 2017, doi:10.5065/d60863p5.

Holton, J. R., 1967: The diurnal boundary layer wind oscillation above sloping terrain. *Tellus*, **19**, 199–205, https://doi.org/10.1111/j.2153-3490.1967.tb01473.x.

Hu, X.-M., P. M. Klein, and M. Xue, 2013: Evaluation of the updated YSU planetary boundary layer scheme within WRF for wind resource and air quality assessments. *J. Geophys. Res. Atmos.*, **118**, 10 490–10 505, https://doi.org/10.1002/jgrd.50823.

Klein, P. M., X.-M. Hu, and M. Xue, 2014: Impacts of mixing processes in nocturnal atmospheric boundary layer on urban ozone concentrations. *Bound.-Layer Meteor.*, **150**, 107–130, https://doi.org/10.1007/s10546-013-9864-4.

——, ——, A. Shapiro, and M. Xue, 2016: Linkages between boundary-layer structure and the development of nocturnal low-level jets in central Oklahoma. *Bound.-Layer Meteor.*, **158**, 383–408, https://doi.org/10.1007/s10546-015-0097-6.

Maddox, R. A., 1983: Large-scale meteorological conditions associated with midlatitude, mesoscale convective complexes. *Mon. Wea. Rev.*, **111**, 1475–1493, https://doi.org/10.1175/1520-0493(1983)111<1475:LSMCAW>2.0.CO;2.

Markowski, P., and Y. Richardson, 2010: *Mesoscale Meteorology in Midlatitudes*. John Wiley & Sons, 430 pp., doi:10.1002/9780470682104.

Mirocha, J. D., M. D. Simpson, J. D. Fast, L. K. Berg, and R. Baskett, 2016: Investigation of boundary-layer wind predictions during nocturnal low-level jet events using the Weather Research and Forecasting model. *Wind Energy*, **19**, 739–762, https://doi.org/10.1002/we.1862.

Ohya, Y., R. Nakamura, and T. Uchida, 2008: Intermittent bursting of turbulence in a stable boundary layer with low-level jet. *Bound.-Layer Meteor.*, **126**, 349–363, https://doi.org/10.1007/s10546-007-9245-y.

Paegle, J., and G. E. Rasch, 1973: Three-dimensional characteristics of diurnally varying boundary-layer flows. *Mon. Wea. Rev.*, **101**, 746–756, https://doi.org/10.1175/1520-0493(1973)101<0746:TCODVB>2.3.CO;2.

Pan, Z., M. Segal, and R. W. Arritt, 2004: Role of topography in forcing low-level jets in the central United States during the 1993 flood-altered terrain simulations. *Mon. Wea. Rev.*, **132**, 396–403, https://doi.org/10.1175/1520-0493(2004)132<0396:ROTIFL>2.0.CO;2.

Parish, T. R., 2016: A comparative study of the 3 June 2015 Great Plains low-level jet. *Mon. Wea. Rev.*, **144**, 2963–2979, https://doi.org/10.1175/MWR-D-16-0071.1.

——, 2017: On the forcing of the summertime Great Plains low-level jet. *J. Atmos. Sci.*, **74**, 3937–3953, https://doi.org/10.1175/JAS-D-17-0059.1.

——, and R. D. Clark, 2017: On the initiation of the 20 June 2015 Great Plains low-level jet. *J. Appl. Meteor. Climatol.*, **56**, 1883–1895, https://doi.org/10.1175/JAMC-D-16-0187.1.

Päschke, E., R. Leinweber, and V. Lehmann, 2015: An assessment of the performance of a 1.5 μm doppler lidar for operational vertical wind profiling based on a 1-year trial. *Atmos. Meas. Tech.*, **8**, 2251–2266, https://doi.org/10.5194/amt-8-2251-2015.

Pitchford, K. L., and J. London, 1962: The low-level jet as related to nocturnal thunderstorms over Midwest United States. *J. Appl. Meteor.*, **1**, 43–47, https://doi.org/10.1175/1520-0450(1962)001<0043:TLLJAR>2.0.CO;2.

Shapiro, A., and E. Fedorovich, 2009: Nocturnal low-level jet over a shallow slope. *Acta Geophys.*, **57**, 950–980, https://doi.org/10.2478/s11600-009-0026-5.

——, and ——, 2010: Analytical description of a nocturnal low-level jet. *Quart. J. Roy. Meteor. Soc.*, **136**, 1255–1262, https://doi.org/10.1002/qj.628.

——, ——, and S. Rahimi, 2016: A unified theory for the Great Plains nocturnal low-level jet. *J. Atmos. Sci.*, **73**, 3037–3057, https://doi.org/10.1175/JAS-D-15-0307.1.

Skamarock, W. C., and Coauthors, 2008: A description of the Advanced Research WRF version 3. NCAR Tech. Note NCAR/TN-475+STR, 113 pp., https://doi.org/10.5065/D68S4MVH.

Smith, E., J. Gibbs, E. Fedorovich, and P. M. Klein, 2018: WRF Model study of the Great Plains low-level jet: Effects of grid spacing and boundary layer parameterization. *J. Appl. Meteor. Climatol.*, **57**, 2375–2397, https://doi.org/10.1175/JAMC-D-17-0361.1.

Song, J., K. Liao, R. L. Coulter, and B. M. Lesht, 2005: Climatology of the low-level jet at the Southern Great Plains atmospheric boundary layer experiments site. *J. Appl. Meteor. Climatol.*, **44**, 1593–1606, https://doi.org/10.1175/JAM2294.1.

Steeneveld, G., T. Mauritsen, E. De Bruijn, J. Vilà-Guerau de Arellano, G. Svensson, and A. Holtslag, 2008: Evaluation of limited-area models for the representation of the diurnal cycle and contrasting nights in CASES-99. *J. Appl. Meteor. Climatol.*, **47**, 869–887, https://doi.org/10.1175/2007JAMC1702.1.

Stensrud, D. J., 1996: Importance of low-level jets to climate: A review. *J. Climate*, **9**, 1698–1711, https://doi.org/10.1175/1520-0442(1996)009<1698:IOLLJT>2.0.CO;2.

Storm, B., J. Dudhia, S. Basu, A. Swift, and I. Giammanco, 2009: Evaluation of the Weather Research and Forecasting model on forecasting low-level jets: Implications for wind energy. *Wind Energy*, **12**, 81–90, https://doi.org/10.1002/we.288.

Sukoriansky, S., B. Galperin, and V. Perov, 2005: Application of a new spectral theory of stably stratified turbulence to the atmospheric boundary layer over sea ice. *Bound.-Layer Meteor.*, **117**, 231–257, https://doi.org/10.1007/s10546-004-6848-4.

Sun, J., L. Mahrt, R. M. Banta, and Y. L. Pichugina, 2012: Turbulence regimes and turbulence intermittency in the stable boundary layer during CASES-99. *J. Atmos. Sci.*, **69**, 338–351, https://doi.org/10.1175/JAS-D-11-082.1.

Trier, S. B., C. A. Davis, D. A. Ahijevych, M. L. Weisman, and G. H. Bryan, 2006: Mechanisms supporting long-lived episodes of propagating nocturnal convection within a 7-day WRF Model simulation. *J. Atmos. Sci.*, **63**, 2437–2461, https://doi.org/10.1175/JAS3768.1.

Turner, D., 2015: FP3 AERIoe thermodynamic profile retrieval data, version 2.0. UCAR/NCAR, Earth Observing Laboratory, accessed 1 August 2017, doi:10.5065/d6z31wv0.

——, 2016a: FP2 AERIoe thermodynamic profile retrieval data, version 1.0. UCAR/NCAR, Earth Observing Laboratory, accessed 1 August 2017, doi:10.5065/d6x63k9k.

——, 2016b: MP1 OU/NSSL CLAMPS AERIoe thermodynamic profile retrieval data, version 1.0. UCAR/NCAR, Earth Observing Laboratory, accessed 1 August 2017, doi:10.5065/d6vq312c.

——, 2016c: MP1 OU/NSSL CLAMPS Doppler lidar VAD wind data, version 1.0. UCAR/NCAR, Earth Observing Laboratory, accessed 1 August 2017, doi:10.5065/d6br8qjh.

——, 2016d: MP1 OU/NSSL CLAMPS Doppler lidar vertical velocity data, version 1.0. UCAR/NCAR, Earth Observing Laboratory, accessed 1 August 2017, doi:10.5065/d6gf0rwh.

——, and U. Löhnert, 2014: Information content and uncertainties in thermodynamic profiles and liquid cloud properties retrieved from the ground-based Atmospheric Emitted Radiance Interferometer (AERI). *J. Appl. Meteor. Climatol.*, **53**, 752–771, https://doi.org/10.1175/JAMC-D-13-0126.1.

Vanderwende, B. J., J. K. Lundquist, M. E. Rhodes, E. S. Takle, and S. L. Irvin, 2015: Observing and simulating the summertime low-level jet in central Iowa. *Mon. Wea. Rev.*, **143**, 2319–2336, https://doi.org/10.1175/MWR-D-14-00325.1.

Walters, C. K., and J. A. Winkler, 2001: Airflow configurations of warm season southerly low-level wind maxima in the Great Plains. Part I: Spatial and temporal characteristics and relationship to convection. *Wea. Forecasting*, **16**, 513–530, https://doi.org/10.1175/1520-0434(2001)016<0513:ACOWSS>2.0.CO;2.

Wexler, H., 1961: A boundary layer interpretation of the low-level jet. *Tellus*, **13**, 368–378, https://doi.org/10.3402/tellusa.v13i3.9513.

Whiteman, C. D., X. Bian, and S. Zhong, 1997: Low-level jet climatology from enhanced rawinsonde observations at a site in the southern Great Plains. *J. Appl. Meteor.*, **36**, 1363–1376, https://doi.org/10.1175/1520-0450(1997)036<1363:LLJCFE>2.0.CO;2.

Zhong, S., J. D. Fast, and X. Bian, 1996: A case study of the Great Plains low-level jet using wind profiler network data and a high-resolution mesoscale model. *Mon. Wea. Rev.*, **124**, 785–806, https://doi.org/10.1175/1520-0493(1996)124<0785:ACSOTG>2.0.CO;2.